



**HAL**  
open science

# Internal structure of the oceanic lithosphere at a melt-starved ultra-slow-spreading mid-ocean ridge: insights from 2-D seismic data

Ekeabino Momoh, Mathilde Cannat, Sylvie Leroy

## ► To cite this version:

Ekeabino Momoh, Mathilde Cannat, Sylvie Leroy. Internal structure of the oceanic lithosphere at a melt-starved ultra-slow-spreading mid-ocean ridge: insights from 2-D seismic data. *Geochemistry, Geophysics, Geosystems*, 2020, 21 (2), pp.e2019GC008540. 10.1029/2019GC008540 . hal-02429984

**HAL Id: hal-02429984**

**<https://hal.science/hal-02429984>**

Submitted on 6 Aug 2020

**HAL** is a multi-disciplinary open access archive for the deposit and dissemination of scientific research documents, whether they are published or not. The documents may come from teaching and research institutions in France or abroad, or from public or private research centers.

L'archive ouverte pluridisciplinaire **HAL**, est destinée au dépôt et à la diffusion de documents scientifiques de niveau recherche, publiés ou non, émanant des établissements d'enseignement et de recherche français ou étrangers, des laboratoires publics ou privés.

# Geochemistry, Geophysics, Geosystems

## RESEARCH ARTICLE

10.1029/2019GC008540

### Key Points:

- Seismic reflectivity structure of amagmatic spreading corridor reveals signatures of possible flip-flop detachment faults
- Detachment faults are steep-dipping ( $>45^\circ$ ) in the upper 5 km of the ultramafic basement at the early stages and more shallow dipping ( $25^\circ$ ) after developing offsets  $>10$  km
- Seismic reflectivity structure consistent with two-phase accretion history: (1) tectonic exhumation in the footwall of a detachment fault, and (2) further faulting, alteration, and magmatic infiltration in the hanging wall of the next detachment fault

### Supporting Information:

- Supporting Information S1
- Figure S1
- Figure S2
- Figure S3
- Figure S4
- Figure S5
- Figure S6
- Figure S7

### Correspondence to:

E. Momoh,  
momoh@ipgp.fr

### Citation:

Momoh, E., Cannat, M., & Leroy, S. (2020). Internal structure of the oceanic lithosphere at a melt-starved ultraslow-spreading mid-ocean ridge: Insights from 2-D seismic data. *Geochemistry, Geophysics, Geosystems*, 21, e2019GC008540. <https://doi.org/10.1029/2019GC008540>

Received 10 JUL 2019

Accepted 20 DEC 2019

Accepted article online 22 DEC 2019

©2019. American Geophysical Union.  
All Rights Reserved.

## Internal Structure of the Oceanic Lithosphere at a Melt-Starved Ultraslow-Spreading Mid-Ocean Ridge: Insights From 2-D Seismic Data

Ekeabino Momoh<sup>1</sup>, Mathilde Cannat<sup>1</sup>, and Sylvie Leroy<sup>2</sup>

<sup>1</sup>Geoscience Marines, Institut de Physique du Globe de Paris, UMR 7154-CNRS, Université de Paris, Paris, France,

<sup>2</sup>Sorbonne Université, CNRS ITeP, Institut des Sciences de la Terre de Paris, Paris, France

**Abstract** Extensive outcrops of serpentized peridotite in melt-starved spreading corridors of the ultraslow easternmost Southwest Indian Ridge are hypothesized to be due to slip on successive long-offset normal faults that alternate polarity (flip-flop detachment faults). We investigate the nature of the oceanic crust which forms under these conditions, using seismic reflection data acquired during the SISMOSMOOTH 2014 cruise. Using 3-D binning, the seismic profiles were binned elastically, while three of the profiles shot closely were merged into one to take advantage of the larger air gun source volume. Using a poststack imaging sequence, we observe several types of reflectors at crustal and infracrustal depths, in the axial valley and off-axis. Correlating our seismic observations with Residual Mantle Bouguer gravity anomalies and seafloor observations, we find that our results are explicable in the framework of the flip-flop hypothesis of detachment faulting. Reflectors imaged down to 5 km into the basement and interpreted as due to damaged zones outlining the detachment faults dip  $50^\circ$  at the early stages, while at late stages after developing offsets  $>10$  km, they dip  $25^\circ$ . Other reflectors observed in the crust are interpreted as moderate offset ( $<200$  m) normal faults accommodating deformation and alteration in the hanging wall and channeling the sparse melt to the seafloor. We interpret these and other observed seismic reflectors in the frame of a two-phase evolutionary sequence over the lifetime of two successive flip-flop detachment faults: exhumation, footwall flexure, damage, serpentization, and incipient magmatism in the footwall of one detachment fault; followed by further tectonic damage, alteration, and incipient magmatism in the hanging wall of the next detachment fault.

## 1. Introduction

Outcrops of altered mantle-derived peridotites on the seafloor of slow-spreading ridges are attributed to exhumation in the footwall of long-offset normal faults (also called detachment faults) which is now known to be a unique mode of seafloor spreading (Cann et al., 1997; Cannat, 1993; Dick et al., 2008; Escartin et al., 2008; Karson & Dick, 1983). Oceanic core complexes (OCCs), that is, domal-shaped structural features, interpreted as the exhumed footwall of detachment faults are common indicators on bathymetric maps of melt-poor sections of slow-spreading ridges (Cann et al., 1997; Smith et al., 2006). The exposed surfaces of most OCCs mapped in the Mid-Atlantic Ridge (MAR), and in magmatically active regions at the slower spreading Southwest Indian Ridge (SWIR) are characterized by spreading-parallel corrugations (Cann et al., 1997), in contrast to some of the OCCs observed at nearly amagmatic corridors of the SWIR (Cannat et al., 2006; Sauter et al., 2013). The distribution of seismicity indicates that detachment faults are concave-downward (deMartin et al., 2007; Parnell-Turner et al., 2017; Yu et al., 2013) and geological evidence (MacLeod et al., 2002, 2009; Smith et al., 2006) and paleomagnetic observations on re-oriented core samples (Garces & Gee, 2007; Morris et al., 2009) confirm flexural rollback of up to  $70^\circ$  of the footwall of corrugated MAR detachment faults. Seafloor sampling and drill-cores targeted at corrugated OCCs in the MAR such as the Kane OCC and Atlantis Massif, recovered serpentized peridotites and 30–40% gabbros and basalts (Blackman et al., 2002; Dick et al., 2008). Sampling of the seafloor at the noncorrugated SWIR OCCs, by contrast, has yielded 90% serpentized peridotites (Sauter et al., 2013). Closely related to detachment faulting at melt-poor sections of slow-spreading mid-ocean ridges is serpentization of exhumed rocks (hydration of mantle minerals, especially olivine, to serpentine). This process occurs at temperatures  $<400^\circ\text{C}$  (Fruh-Green et al., 2004) and is probably facilitated by fractures associated with the detachment faults (Andreani et al., 2007; Cannat et al., 2010; Roumejon & Cannat, 2014). Sampling and geological

observations are, however, restricted to near the exhumed detachment fault surfaces, and the extent of serpentinization on a crustal scale is therefore not well constrained from direct geological observations. The same is true for the depth distribution and abundance of magmatic rocks that form intrusions into the ultramafic basement (Cannat, 1993), and for the distribution and geometry of faults. Geophysical techniques are therefore key to address these questions and get a better understanding of the tectonic and magmatic processes that shape slow and ultraslow spreading oceanic lithosphere.

Seismic tomography studies in domains of the MAR, where corrugated OCCs have been mapped, indicate a thin crust ( $\leq 5$  km), for example, Canales et al. (2008), Dunn et al. (2017), Xu et al. (2009); and elevated RMBA (Cannat et al., 1995), which suggests that the melt supply is moderate. Compressional wave tomography velocity models in melt-poor domains of the SWIR indicate that even though the melt supply is low, the geophysical crustal thickness is non-zero (Momoh et al., 2017; Muller et al., 1997), suggesting that crustal-type seismic velocities result from extensive tectonic damage and hydrothermal alteration of the exhumed ultramafic rocks and intruding gabbros.

While seismic tomography provides insight into the velocity structure in these moderate to nearly zero-melt areas, the seismic reflectivity structure of OCC-type oceanic lithosphere is not well known. A natural laboratory where tectonically dominated accretion in OCC-type oceanic lithosphere can be investigated is the melt-poor domain near the easternmost SWIR (64°E of longitude), where seismic reflection and refraction data have been acquired (Leroy et al., 2015).

The Southwest Indian Ridge forms the plate boundary between Africa and Antarctica plates. It has a full spreading rate of 14 mm/year (Patriat & Segoun, 1988). It is classified, along with the Gakkel Ridge in the Arctic, as an ultraslow spreading ridge (Dick et al., 2003). The easternmost portion of the Southwest Indian Ridge, east of the Melville Fracture Zone (60°E of longitude) between 61°E and 65°E of longitude, and 27°S and 28°S of latitude, represents an end-member of the global mid-ocean ridge system documented in terms of low regional melt supply on average. The low melt supply is inferred from large regional ridge depths, positive gravity anomalies, sodium content of basalts, and thinner than average seismic crust (Cannat et al., 1999, 2008; Minshull et al., 2006; Muller et al., 1999).

The 64°E nearly amagmatic corridor has been extensively studied by dredging, bathymetric and sidescan sonar surveys (Sauter et al., 2013), seismic reflection and refraction (Momoh et al., 2017; and this study), and a recent Remotely Operated Vehicle exploration cruise (Cannat et al., 2017). The seafloor bathymetry map in our study area (Figure 1) shows the nearly amagmatic corridor (“smooth seafloor”), which is centered around 64°36'E. This smooth seafloor corridor forms a spreading domain 50 to 100 km wide in the along-axis direction, between the two adjacent magmatically more robust ridge sections with focused axial magmatism (Cannat et al., 2006). Nearly amagmatic seafloor there forms broad ridges (500 to 1,000 m high) that have been interpreted as OCCs formed by successive asymmetric rolling-hinge axial detachment faults which continuously flip polarity (hence referred to as flip-flop detachment faulting; Reston & McDermott, 2011) over the past 8 Mya (Sauter et al., 2013).

The exposed part of the proposed flip-flop detachment fault system (Sauter et al., 2013) is partitioned (Figure 1) into an emergence (where the fault intersects the seafloor; picked at the base of the outward facing slopes of each ridge), and a breakaway (where the fault initiated, cutting into the footwall of the previous detachment fault; picked at the apex of inward-facing slopes of each ridge). Seafloor geology indicates that sparse volcanism at the seafloor is spatially associated with faults, and that increased magmatism may contribute to terminating activity on a detachment fault (Sauter et al., 2013). Domains of volcanic seafloor in this smooth seafloor corridor have been shown to be patches of lava and volcanic edifices emplaced directly on the ultramafic seafloor (Sauter et al., 2013). While surface evidence and geological sampling at the easternmost Southwest Indian Ridge allude to features not replicated in other mid-ocean ridge settings of low regional melt supply, little is known of the internal structure of the subseafloor.

Momoh et al. (2017) analyzed seismic reflection data from a narrow 3-D box shot in the axial valley of a melt-poor SWIR domain near 64°E of longitude (3-D box outline shown in Figure 1 and identified reflectors dipping 45–55° down to 5 km below the seafloor (the resolution limit for the seismic experiment) beneath the trace of the emergence of the presently active axial detachment fault, and interpreted them as due to tectonic damage in the basement. In the hanging wall next to this damage zone, the seismic crust (defined by the compressional wave velocity model  $< 7.5$  km/s) is thicker (5 km) than further away from it (4 km). This

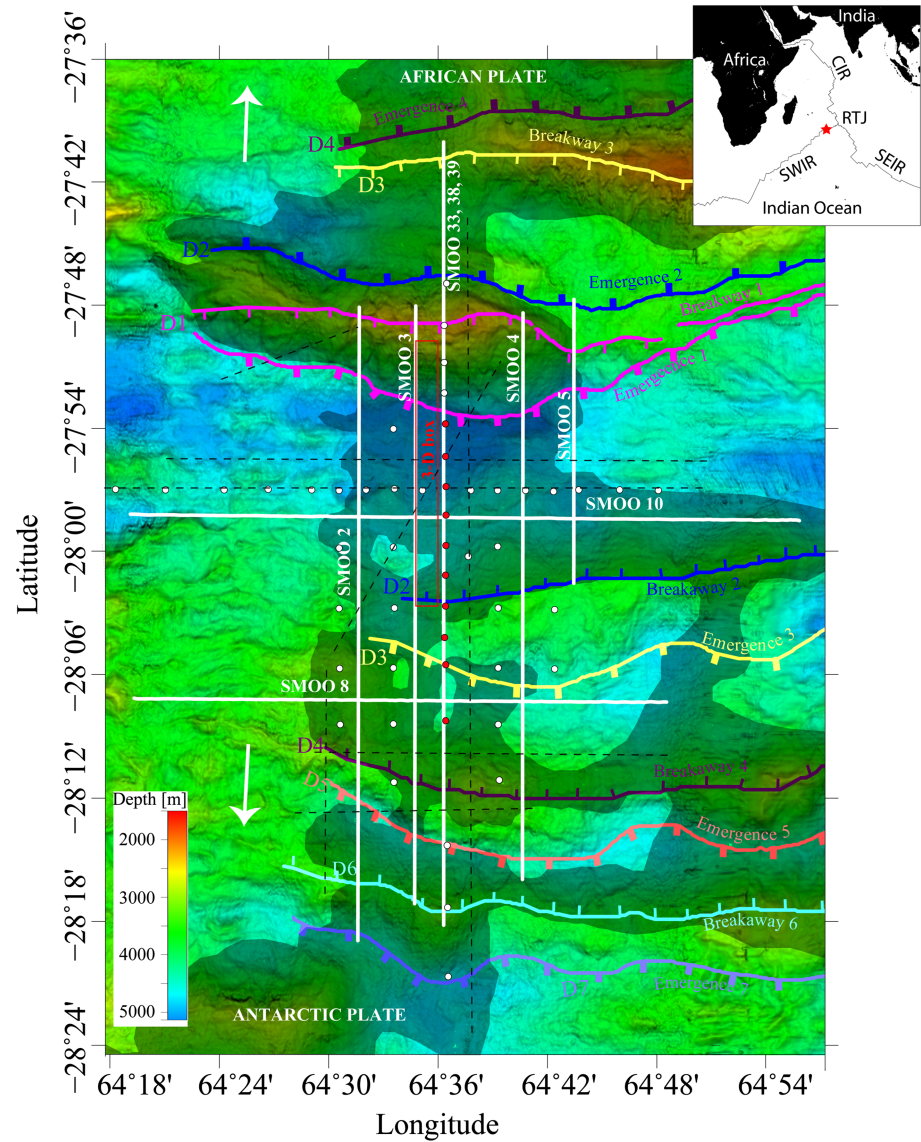


**Figure 1.** Bathymetric map of our study area with the traces of the emergence and breakaway of successive detachment faults (Cannat et al., 2019). Plate separation is approximately north-south (indicated by the white arrows). The darkened area indicates the preponderance of ultramafic rocks (“smooth seafloor”), otherwise the seafloor is volcanic. The boundaries between volcanic and smooth seafloor are constrained by the interpretation of acoustic backscatter image, Residual Mantle Bouguer Gravity Anomaly (RMBA) and the sample types recovered from dredges (Cannat et al., 2006; Sauter et al., 2013). The active detachment fault emergence is shown in purple at the base of the high relief (2 km high) OCC centered at 27°51’S of latitude and 64°36’E of longitude and dips south under the Antarctic plate. The exhumed and eroded portion of the fault system is designated by D1 (corresponding to the extent defined by the surface emergence [indicated by thick tick lines] and the breakaway [thin tick lines] of detachment fault 1). The breakaway of each fault represents the part where the fault initially broke the seafloor before exhumation, interpreted at the apex of each broad ridge. The other colored lines and associated labels indicate traces of the emergence and breakaway of inactive detachment faults with increasing age (corresponding to detachment faults D2, D3, D4, D5, D6, and D7, respectively). The seismic shot profiles are shown by white lines with their respective names, while the 3-D box (Momoh et al., 2017) is indicated in red rectangle. Other seismic shot profiles acquired during the expedition are indicated by dashed lines. The ocean bottom seismometers deployed are shown in white circles, while the red circles indicate the available tomography velocity model for this area. The inset shows the location of the study area (red star) in the Southwest Indian Ridge (SWIR). RTJ is the Rodrigues Triple Junction where the Southwest Indian Ridge (SWIR), Southeast Indian Ridge and Central Indian Ridge intersect.

crust has been described as a downward gradient of serpentinization with tectonic damage and small magmatic intrusions (Momoh et al., 2017). Several dipping and subhorizontal reflectors were also imaged in the crustal portion of the hanging wall of the active detachment fault and shallow mantle of the axial valley region and interpreted as minor offset faults and magmatic rocks trapped in the ultramafic basement (Momoh et al., 2017).

In the study presented here, we analyze additional and longer 2-D seismic reflection profiles acquired during the same cruise (SISMOSMOOTH 2014), extending up to 70 km across-axis and 19 km along axis (Leroy et al., 2015). Based on these data, we address questions related to the along-axis structure of the active detachment fault, the distribution of seismic reflectors in the hanging wall of this active detachment fault, and the seismic reflectivity structure of older detachment fault systems. We discuss a conceptual model of the accretion of ultraslow spreading and melt-poor oceanic lithosphere that unifies our seismic reflection observations.

## 2. Data Acquisition and Processing

### 2.1. Data Acquisition

The seismic reflection data utilized in this study were acquired during the SISMOSMOOTH 2014 expedition aboard the French Research Vessel Marion Dufresne (Leroy et al., 2015). The data were shot with an airgun array with a combined volume of 42 L shooting every 50 m and recorded with 360 hydrophones along a streamer 4,500 m long. Of the seismic reflection profiles acquired during the SISMOSMOOTH cruise, nine are reported in this paper (Figure 1), three of which were shot with a larger air gun array volume (111 L) with a shot spacing of 150 m during the ocean bottom seismometers profile shooting (Momoh et al., 2017). These three profiles were merged to increase the spatial sampling and take advantage of the increased source volume.

The profiles (shown in Figure 1) sample domains with ages up to 6 Mya (Cannat et al., 2006). Across-axis profiles SMOO 2 and SMOO 5 (Figure 1) are positioned near the transition to more volcanic seafloor in the west and east, respectively. Across-axis profile SMOO 4 cuts through a large patch of volcanic seafloor located south of the inferred breakaway of detachment fault 2 (D2; while D1 is the presently active south-dipping detachment fault). Along-axis profile SMOO 8 cuts into seafloor about 3 Mya while along-axis profile SMOO 10 cuts into the present-day axial domain. The details of the data acquisition are summarized in Table 1.

On the streamer, 17 compasses were placed on birds 300 m apart, which recorded angular orientations that were used to compute positions for the hydrophones. The angles were interpolated to 12.5 m (receiver group spacing) by assuming a smooth variation between the angles. The latitude and longitude values from the global positioning systems on the vessel were converted to local eastings and northings, which were used to compute the eastings and northings for each receiver. In Table S1 in the supporting information, the coordinates of the sources, receivers, and profile lengths are summarized for the individual seismic lines reported in this paper.

### 2.2. Data Analysis

The profiles shot in the across-axis direction were binned and the inline with the highest number of traces were passed for processing. For SMOO 2, SMOO 3, SMOO 4 (shown in the supporting information) and SMOO 5 (shot with the 42 L air gun volume), the common-midpoint gathers are binned 100 m between inlines, and 6.75 m between crosslines. For bins which are underfilled, traces are scanned at individual offsets across bins to compensate for missing traces (flexible binning) at those offsets in the bin under consideration (Yilmaz, 2001). For the flexible binning in this instance, an allowance of 200 m between inlines was made and 12.5 m between crosslines.

Traces further away from this maximum limit were not used during subsequent processing. This procedure allows one to exclude extraneous data by assuming arbitrary straight line geometry and ignoring the impact of feathering (Seher et al., 2010), or applying line projections (Nedimovic & West, 2003). Since the distance between respective seismic profiles ranges between 2.5 and 5 km, there was no mixing of data from different profiles, even though these lines were binned simultaneously, that is, there was no streamer feathering up to 2.5 km.

**Table 1**  
*Data Acquisition Parameters*

Line ID	SMOO 2	
	SMOO 3	
	SMOO 4	SMOO 33
	SMOO 5	SMOO 38
	SMOO 8	SMOO 39
	SMOO 10	
Source volume	43.02 L	111 L
Source interval	50 m	150 m
Source depth	10–14 m	12–18 m
Streamer length	4,500 m	4,500 m
Streamer depth	18 m	22.5 m

The three profiles which were shot in close proximity (SMOO 33, SMOO 38, and SMOO 39) were combined into a single profile. The streamer was deployed at a depth of 22.5 m and shot with a 6,790 in<sup>3</sup> (111 L) air gun array volume with a shot interval of 150 m. The common midpoint fold is 15, which is sub-optimal for imaging. To take advantage of the larger source volume, the three seismic profiles were combined into 1 by 3-D binning. In setting up the quasi-3-D geometry, we binned 175 m in the inline direction by 6.25 m in the crossline direction. This was extended elastically to 350 and 12.5 m in the inline and crossline directions, respectively. In Figure S1, we demonstrate the strategy for binning the three seismic profiles and the fold for static and dynamic binning. After binning, we observe that two inlines had optimum fold (of 45), we therefore extracted one of the inlines and processed it as a 2-D profile. We also extracted the

inline with the optimum fold for SMOO 2, SMOO 3, SMOO 4, and SMOO 5, even though these profiles were respectively acquired along a single sail line. For quality control, we extract the individual inlines of the combined lines SMOO 33, SMOO 38, and SMOO 39 to examine possible variations in the stacked images (Figures S2a–S2c), respectively). Despite the differences in the shooting directions, the features observed on the three profiles are similarly reproduced (the dipping reflector between crossline numbers 6,200–7,000, and up to 7 s two-way time (TWT), for instance).

The processing strategy for all the profiles is demonstrated using the combined line as example (hereafter referred to by SMOO 33). The combination of three lines attempted to increase the fold by a factor of 3, and therefore improve the signal-to-noise ratio by a factor of 1.73. A poststack processing sequence is adopted here, and it is geared toward noise suppression, amplitude corrections, traveltimes corrections, and imaging. The amplitude corrections include spherical divergence correction and predictive deconvolution; travel-time corrections include normal moveout and dip moveout corrections, which are the first-two steps in the imaging sequence.

We compared stacking using root-mean-squared velocities derived from the coincident tomography velocity model and using the semblance-based velocity analysis. The sparsity of seismic reflectors below the seafloor provided insufficient constraints for the semblance-based velocity analyses. Therefore, stacking velocities were constrained on individual seismic profiles based on the tomography velocity model (where subseafloor reflectors are absent) and on reflectors and features observed on neighboring profiles where reflectors are observed. An example of a common midpoint supergather and stacking velocity is shown in Figure S3. The far-offset traces were zeroed before stacking midpoint gathers.

The dip moveout correction implemented here is in the f-k domain where each time dip maps to a single radial line (Deregowski & Rocca, 1981; Hale, 1984). Prior to transforming the dip moveout elliptical operator to the f-k domain, the time coordinate is transformed to a log of time (Bolondi et al., 1982; Cabrera & Levy, 1989). The seismic section in the common offset domain after normal moveout correction is transformed to a log-of-time coordinate as well, which is equivalent to a simple stretching of the time axis. The sample rate in the log-stretch domain is 8 ms and this was adequate to insure for proper temporal sampling. The resulting data are transformed to the f-k domain where the data are multiplied by the DMO operator similarly transformed. In this domain, the correction corresponds to a phase shift. The corrected-data are transformed back to the time-domain where the time coordinate is unstretched by an inverse exponential law. The log-stretch dip moveout correction of Liner (1990) was adopted for the data presented here. The effect of the dip-moveout correction in our data is the reduction of the seafloor diffraction tails, which dominated the data from the seafloor. This comparison is shown for stacked inline in the axial domain before DMO correction (Figure 2a) and after DMO correction (Figure 2b).

Predictive deconvolution was used to reduce the short-period multiples. We used an operator length of 400 ms and a predictive lag of 36 ms (third zero-crossing of the autocorrelogram). The noise suppression includes trapezoidal band-pass filtering, prestack (shot) dip filtering, and 11-trace poststack mild lateral smoothing to suppress high-frequency residual noise. The result of the predictive deconvolution, post-deconvolution band-pass filter, and lateral smoothing is shown in Figure 2c. For imaging, we used the explicit finite difference algorithm (Claerbout & Johnson, 1971; Loewenthal et al., 1976), which numerically reconstructs the

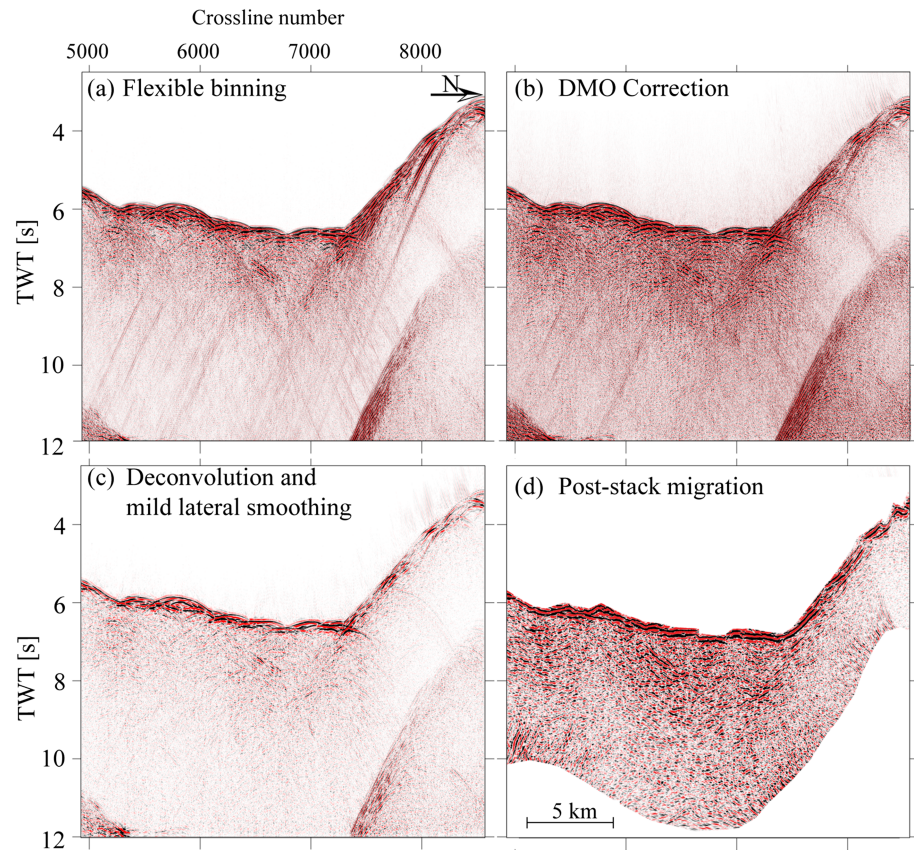


**Figure 2.** Example of seismic reflection data processing on 2-D lines. (a) Line after flexible binning. Strong diffraction tails due to the seafloor are observed, for instance the arrows point to two of them. (b) After dip-moveout correction. The diffraction limbs in (a) are no longer apparent in the first 2 s TWT. (c) After predictive deconvolution and mild lateral filtering. The seafloor reflection is relatively compressed. (d) After post-stack migration and muting of seafloor multiple responses. All figures are plotted on the same scale.

wavefield at different time levels. For effective imaging which was assessed by the collapse of the diffraction hyperbolae on all sections, we found a downward continuation step size of 16 ms and a convolutional filter using 17 points optimally images events up to 55°. The result of the migration is shown in Figure 2d. In all steps, we confined the processing to low frequencies (<35 Hz), as we found to be effective in the quasi-3-D box (Momoh et al., 2017). The key processing steps are listed in Table 2.

### 3. Results

We first present the results from the near-axis domain where we have the most mapping, sampling, geological, and geophysical constraints on the tectonic-volcanic setting. We propose a grouping of the observed reflectors imaged in the across-axis profiles; then on, we attempt to identify these reflectors in the crossing, along-axis profiles, in order to better constrain their true dip. Indications on the probable depth of the observed reflectors are based on the velocity model obtained by Momoh et al. (2017) along a profile that is coincident with seismic reflection profile SMOO 33 (Figure 1). In grouping the reflectors, we include the surface extent of the different detachment fault systems, which we have labeled according to the estimated age of their activity (Cannat et al., 2019); for example, D1, represents the presently active detachment fault system, and D2 represents the penultimate detachment fault and D3 until D7, represents past detachment faults, up to the limit of the corridor investigated in this study.

The time-migrated across-axis profiles (SMOO 2, SMOO 3, SMOO 33, and SMOO 5) are described sequentially from the west of the investigated corridor (Figures 3a–3d). SMOO 4 is shown in Figure S4 in the supporting information. Resolving the seafloor reflection on this profile was challenging due to rough sea

**Table 2**  
*Seismic Reflection Data Processing Steps*

**Pre-stack processing**

Data conversion (from SEG-D) to processing environment  
 Streamer shape reconstruction and preparation of navigation (.P190) files  
 Merge raw data from individual seismic lines with navigation information  
 3-D static binning  
   6.25 m 100 m (SMOO - 2, 3, 5)  
   6.25 m 175 m (SMOO - 33, 38, 39)  
 3-D elastic binning  
   12.5 m 200 m (SMOO - 2, 3, 5)  
   12.5 m 350 m (SMOO- 33, 38, 39)  
 Resample to 4 ms after anti-alias filter, 125 Hz cut-off  
 Mute direct waves  
 Ormsby bandpass filter (3-6-41-55 Hz)  
 Coherency filtering 10 ms/trace  
 Spherical divergence correction  
 Common bin gather sort (45 fold), 6.25 m interval  
 Velocity analysis 1  
 Migration to zero offset (log-stretch dip-moveout correction)  
 Velocity analysis 2  
 Predictive deconvolution: 400 ms operator length, 3rd zero crossing lag  
 Bandpass filter  
 Mean stacking

**Post-stack Processing**

Mean filtering (running average)  
 2-D explicit finite difference time migration

**Post-migration**

Ormsby bandpass filter (3-6-35-42 Hz)  
 Mute below first order multiple  
 Mean filtering (11-trace lateral smoothing)

conditions during acquisition. The line interpretation on the across-axis profiles is shown in Figure 4. The along-axis profiles SMOO 10 and SMOO 8 are shown with indications of the main reflectors in Figure 5. The migrated profiles are shown in Figure S5.

In further presenting the results, we compare reflectors in crossing profiles near axis (Figure 6) and extract the outer inlines of the 3-D box (Momoh et al., 2017) compared with the profiles from the smooth-volcanic corridor in this study as shown in (Figure 6), since the reflectors imaged in the 3-D box are not dissimilar to those imaged on the 2-D profiles bounding the 3-D box, that is, SMOO 3 and SMOO 33 (Figure 4b and 4c).

**3.1. Reflectors in the Near-Axis Domain**

Similar to the narrow 3-D box discussed in Momoh et al. (2017), two categories of dipping reflectors are observed near axis: south dipping reflectors located near the emergence of the active detachment fault (E1; Figures 4 and 6) and reflectors with an apparent northward dip (Figures 4a–4c, 6, and S6). Between these reflectors are apparently subhorizontal reflectors.

The south-dipping reflectors occur between 6.62 and 8.26 s TWT, corresponding to depths of up to 5 km below the seafloor (Figure 8). The depths of reflectors are estimated in the poststack domain by a time-to-depth conversion of the seismic section using the tomography velocity model obtained along a coincident profile (Momoh et al., 2017). These reflectors are offset from each other and from the trace of the emergence of the active fault, and are distributed over a domain that is 490 m to 1.8 km thick, where the narrowest zone is on the eastern boundary of the investigated corridor (SMOO 5;

Figure 4d) and the wider zone on the center of the corridor (SMOO 33; Figure 4c). These reflectors have maximum dips of 50° (Figure 8). Our observations here are consistent with results of the narrow 3-D box where the reflectors observed within 5 km from the seafloor dip 45–60° (Momoh et al., 2017).

The north-dipping reflectors near axis are observed between 5.62 and 7.67 s TWT, and between 6 and 14 km south of the inferred emergence (E1) of the active detachment fault system (whose spatial extent is labeled D1) as shown in SMOO 2, SMOO 3, and SMOO 33 (Figures 4a–4c). These north-dipping reflectors are shallower-dipping toward the west as shown on SMOO 2 (Figure 4a), and they are observed near apparently east-dipping reflectors imaged between 18 and 23 km line distance on the intersecting along-axis profile (SMOO 10 shown in Figure 5a). This is illustrated in Figure 6. Only on one profile (SMOO 2) do we observe a coincidence (in traveltimes and amplitude) between the north-dipping reflectors and an apparently east-dipping reflector.

Apparent south-dipping reflectors are observed near axis on SMOO 5, ~1 s TWT below the seafloor between 6 and 10 km distance from the inferred emergence of the active detachment fault (Figure 4d). These reflectors are not associated with the trace of any emergence or breakaway of detachment faults, but they terminate at the onset of the volcanic seafloor. The extents of the near-axis main dipping reflectors are summarized in Table 3.

From 6.8 to 9.6 km north of the inferred emergence of the active detachment fault, two packages of disjointed north-dipping reflectors are observed between 4.3 and 6 s TWT (Figure 4c). These reflectors, similar to the steepest reflectors imaged conjugate to the active fault, dip 45° (Figure 7).

The subhorizontal reflectors occur between the north and south-dipping reflectors down to 2.5 s TWT below the seafloor (Figure 4c) corresponding to a depth of 4–5 km (Figure 8). We did not find evidence for subhorizontal reflectors within the footwall of the active axial detachment fault. In Momoh et al. (2017), the north-dipping reflectors discussed above terminated on subhorizontal reflectors. The width of the packages of subhorizontal reflectors ranges between 720 m and 1.34 km. We, however, observe that in the eastern boundary

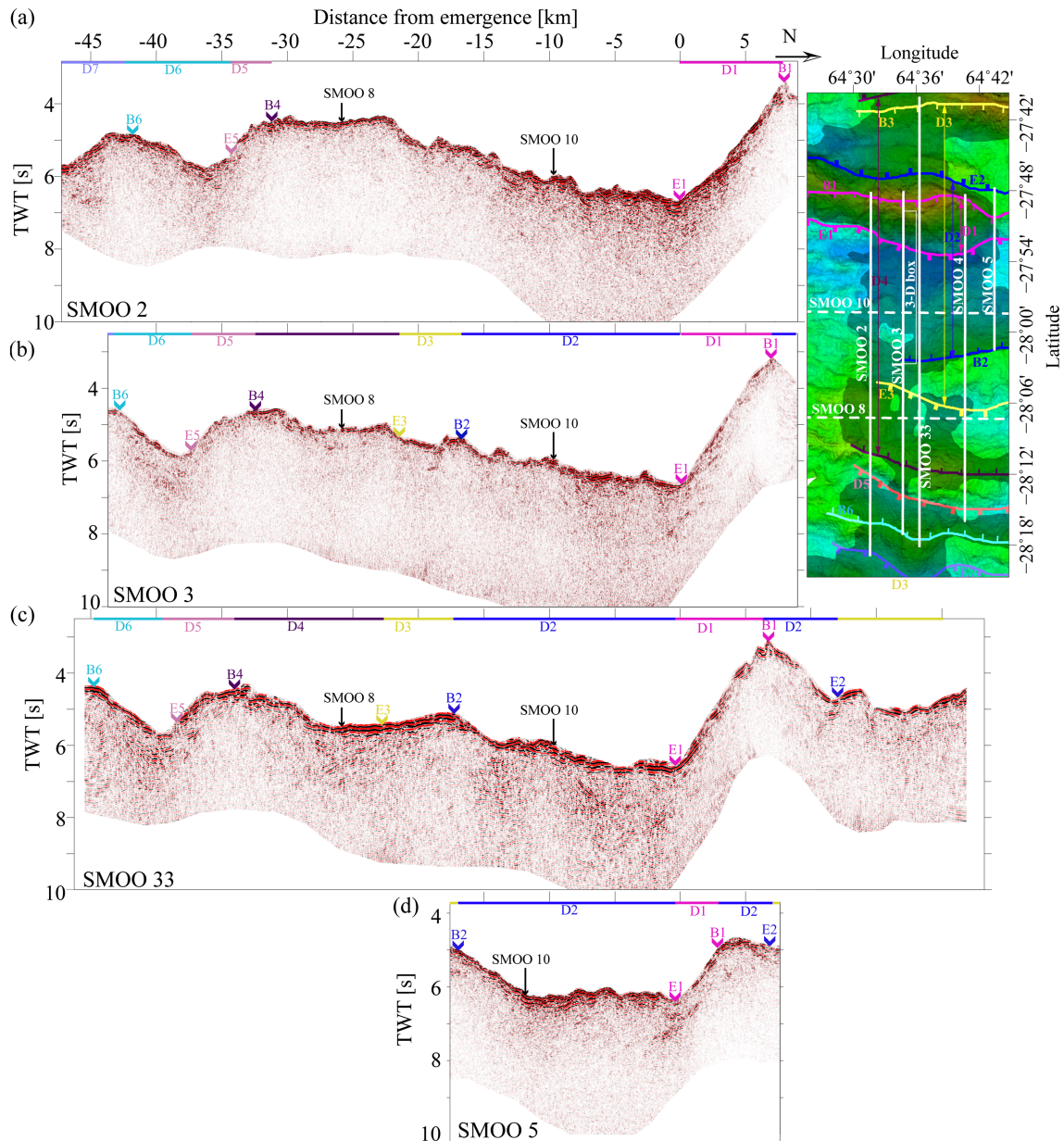


**Figure 3.** Across-axis profiles shown from west to east after 2-D poststack migration. (a) SMOO 2 on the western boundary of the melt-poor corridor. (b) SMOO 3 within the corridor, bordering the narrow 3-D box on the west presented in Momoh et al. (2017). (c) SMOO 33, the combination of three seismic profiles shot in close proximity, 200 m east of the 3-D box. (d) SMOO 5 on the eastern boundary of melt-poor corridor. The markers on the seafloor indicate the approximate locations of the emergence (E1, E2, E3, and E5) and breakaway (B1, B2, B4, and B6) of corresponding detachment faults D1, D2, D3, D4, D5, and D6, respectively. The exhumed footwall of these fault systems are indicated by colored arrows for detachment faults D1, D2, D3, and D4, with successive faults cutting the previous faults thereby displacing the position of the emergence or breakaway depending on the facing direction of the active fault. The seismic profiles displayed in this figure are shown in white on the bathymetric maps while the crossing profiles are shown in white dashed lines. SMOO 4 is shown in Figure S4 in the supporting information, while the crossing profiles are shown in Figure 5.

of the investigated corridor, south-dipping reflectors (with the same apparent dip as the reflectors near the emergence of the active fault) are visible (Figures 4d, 6, and S6).

On the along-axis profile (SMOO 10), isolated packets of subhorizontal reflectors are apparent between 18 and 51 km line distance at 1 s TWT below the seafloor (Figure 5a) without an intersection with the subhorizontal reflectors in the across-axis profiles near axis.

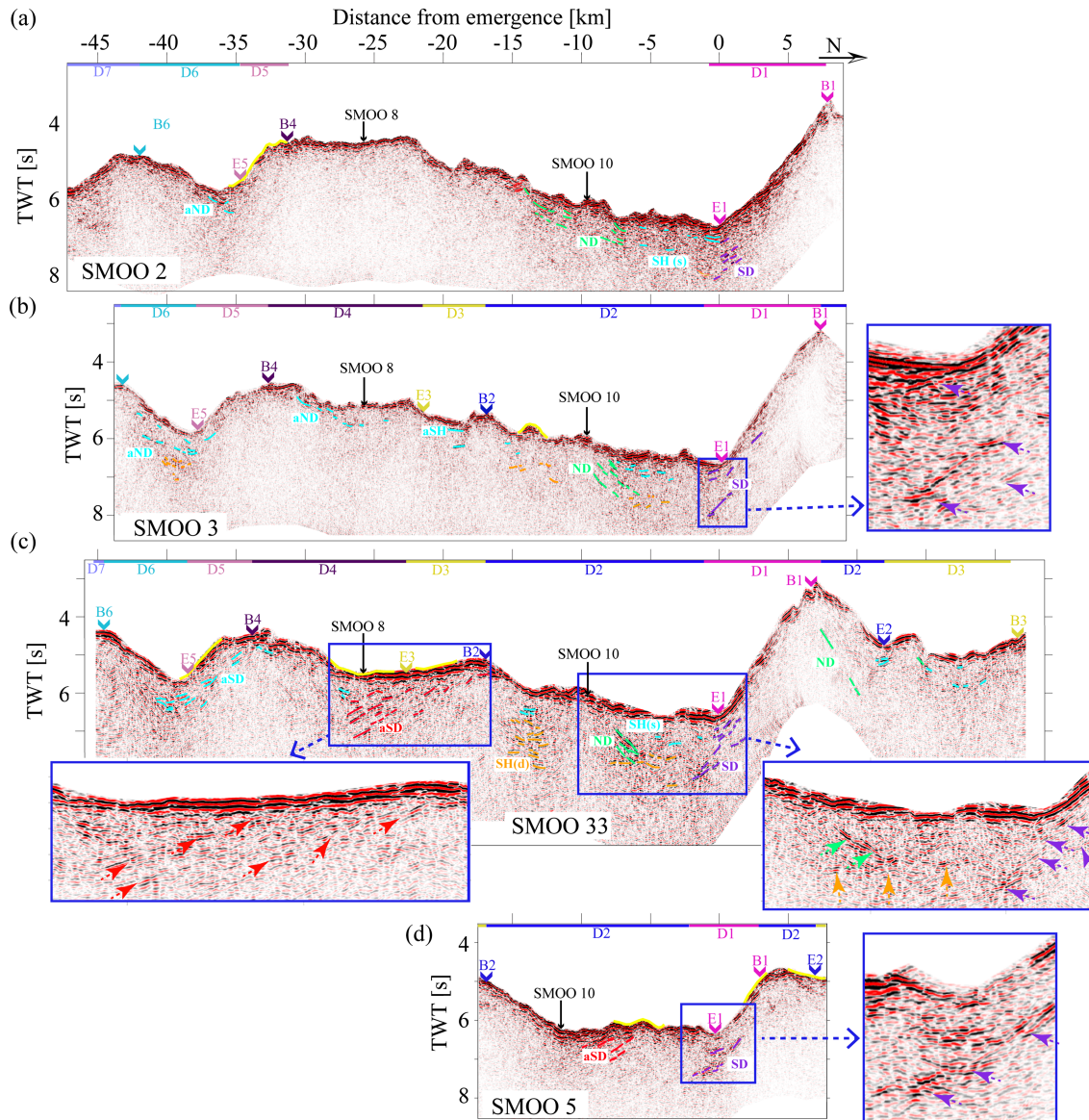


**Figure 4.** Interpretation of 2-D across axis profiles: (a) SMOO 2, (b) SMOO 3, (c) SMOO 33, and (d) SMOO 5. The acronyms on the seafloor indicate the emergence and breakaway of successive detachment faults as shown in Figure 3, and the colored lines atop each figure indicates the spatial extent of the detachment faults interpreted from the bathymetry and from the seismic results. The yellow lines on the seafloor indicate the volcanic patches observed on the seafloor bathymetric map and ground-truthed by seafloor sampling (Cannat et al., 2019; Sauter et al., 2013). The acronyms corresponding to the different line interpretations are as follows: SD = south dipping reflectors; ND = north-dipping reflectors; SH(s) = subhorizontal reflectors (shallow), aSH = apparent subhorizontal reflectors; aSD = apparent south-dipping reflectors, and aND = apparent north-dipping reflectors. Close-up views highlight prevalent reflectors.

### 3.2. Dipping Reflectors in the Antarctic Plate

Reflectors with apparent dips as the seafloor topography can be observed between 35 and 38 km distance from the inferred emergence on SMOO 2, and between 19 and 43 km distance from the inferred emergence on SMOO 3 (Figure 4b). This category of dipping reflectors is also observed on SMOO 33 between 27 and 42 km distance from the inferred emergence (Figure 4c).

The most prominent package of apparently south-dipping reflectors is observed in the Antarctic Plate from 17.5 to 27.5 km distance south of the inferred emergence of the active detachment fault (Figures 4c and 8). This package of reflectors can be observed between 5.24 and 7.15 s TWT. They intersect with apparently subhorizontal reflectors on the crossing along-axis profile (SMOO 8) between 6.5 s and 7.5 s TWT which can be followed from 28 to 43 km line distance (Figure 5b). This intersection is zoomed in on Figure 7. Therefore,

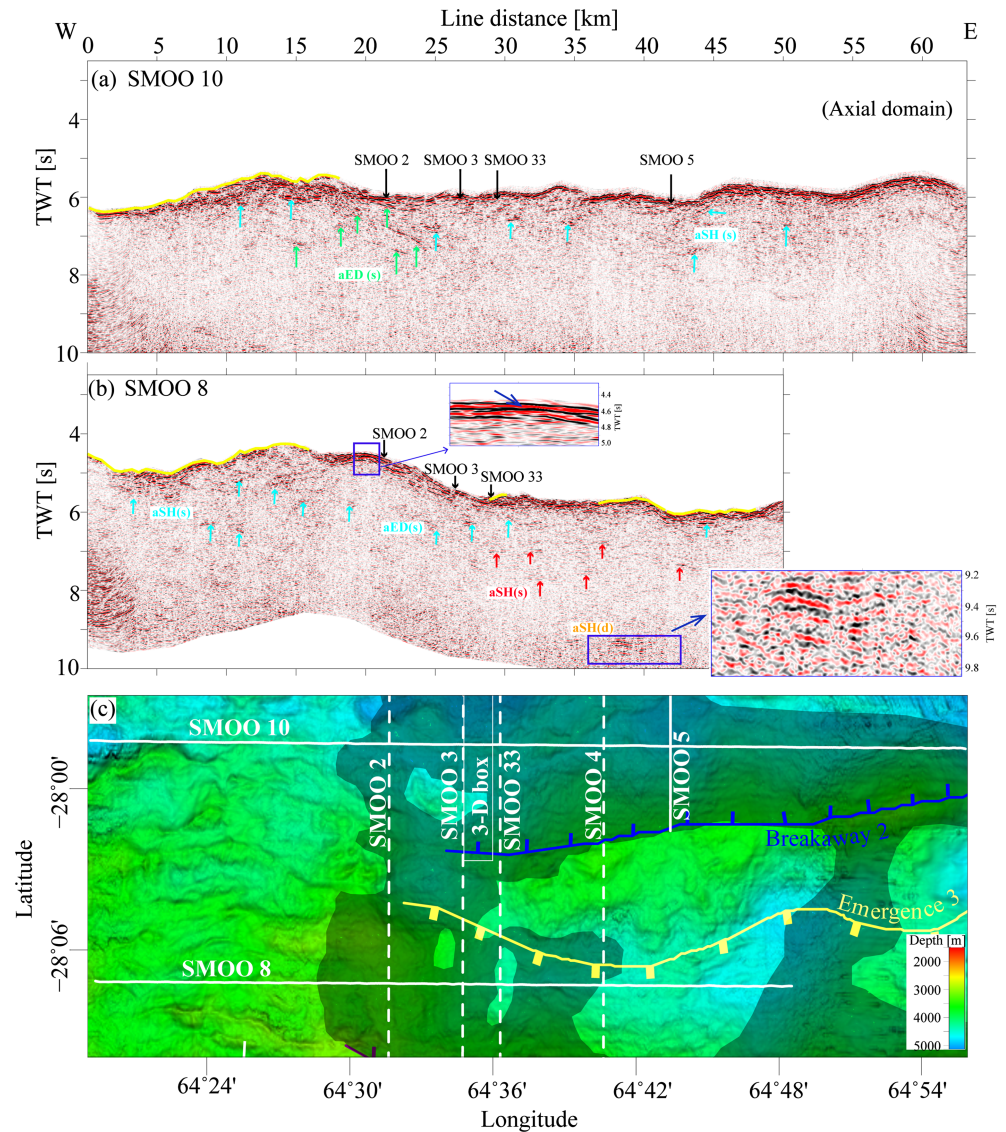


**Figure 5.** Along-axis profiles after 2-D poststack migration shown from north (near-axis) to south (off-axis). Close-up views highlight prevalent reflectors. (a) SMOO 10 with arrows indicating major reflectors: the acronyms represent the time dips of the reflectors observed, for example, aED(s) = apparent east-dipping reflectors (shallow), aSH(s) = apparent subhorizontal reflectors (shallow). The apparent east-dipping reflectors project to volcanic seafloor in the west of this profile. (b) SMOO 8 with reflectors indicated following the same scheme used to indicate reflectors in SMOO 10. aSH(d) = apparent subhorizontal reflectors (deep). The yellow lines on the seafloor correspond to volcanic patches on the seafloor. (c) Detail of bathymetric map showing the locations of the along-axis profiles (highlighted in red). The darkened area indicates smooth seafloor.

we propose that the package of subhorizontal reflectors corresponds to the along-axis signatures of the package of south-dipping reflectors imaged on the across axis profiles. Traces of the package of south-dipping reflectors are also visible on SMOO 4 from 20 to 27.5 km distance south of the inferred emergence of the active detachment fault (Figure S4). In both instances where they are imaged, they project to prominent volcanic patches within the ultramafic corridor. They occur between the inferred emergence and breakaway of the D3 and D2 older detachment fault systems (Figure 4b).

### 3.3. Shallow and Deep Subhorizontal Reflectors in the African and Antarctic Plates

Both in the African and the Antarctic plates, packages of disjointed shallow and apparently subhorizontal reflectors are imaged on all the profiles (Figures 4 and 5). For example, subhorizontal reflectors are

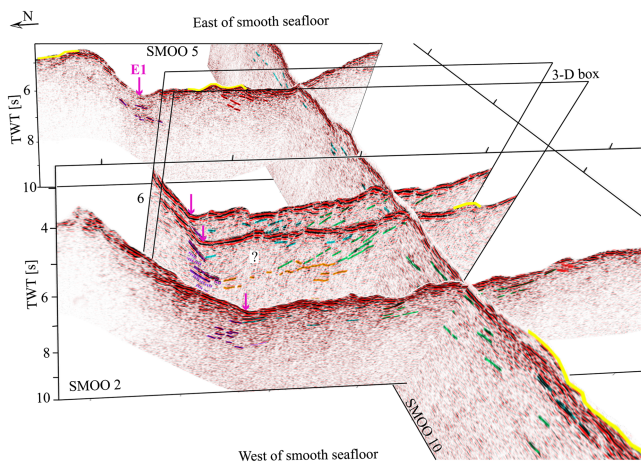


**Figure 6.** Perspective view of along- and across-axis profiles in the near-axis region. View is from the west to the east. The two profiles juxtaposed are inlines from the narrow 3-D box discussed in Momoh et al. (2017). The western inline from the narrow 3-D box is 5 km from SMOO 2, while the eastern inline from the narrow 3-D box is 12.6 km from SMOO 5. Despite these distances, the south-dipping reflectors are consistently imaged. The markers on the seafloor indicate the approximate location of the emergence of the active fault and E1 connotes this emergence. The crossing profile (SMOO 10) shows the possible intersection of the apparently north dipping reflectors across-axis (in green) with apparently east dipping reflectors projecting to volcanic corridors in the west. This observation suggests that the near-axis reflectors are northeastdipping, shallowing westernward.

observed on SMOO 33 between 9 and 16 km distance, south of the inferred emergence at <1 s TWT below the seafloor (Figure 4c). In the Antarctic Plate, apparently subhorizontal reflectors are also observed on SMOO 8 (Figure 5b) between 5 and 20 km line distance. Subhorizontal reflectors are ubiquitous beneath volcanic and smooth seafloor as shown in the crossing profiles (Figure 5b).

The deepest package of apparently subhorizontal reflectors is imaged between 8.74 and 9.77 s TWT between 34.13 and 43.93 km line distance along profile SMOO 8 (Figure 5b). Using the compressional-wave velocity found for this area (Momoh et al., 2017), the first 2 s (from the seafloor; 5.74 s two-way time) correspond to 5 km below the seafloor. The top of this cluster of reflectors occurs at 8.82 s giving a depth of at least 9.3 km below the seafloor using an average velocity of 8 km/s.

This cluster of reflectors therefore occurs within the mantle. From the zoomed panels on these reflectors and the seafloor (inset in Figure 5b), it can be observed that the latter are lower frequency compared to the seafloor reflection. Two distinct packages can be isolated: an upper package which is relatively higher frequency and appears separated from a bottom, lower-frequency package. Although the waveforms are complex probably due to interference between different reflector signatures, comparing the polarity of the main lobe of the lower package and the seafloor indicates that the polarities are opposite (note highlighted portions in the zoomed insets of Figure 5b). This alludes to a possible decrease in velocity and/or density. The slightly higher-frequency reflector observed at 9.6 s in the zoomed panel seems to follow the polarity of the seafloor reflector,

which suggests an increase in velocity and/or density. Using the time interval between reflectors (8.74–9.77 s TWT), and mantle velocities (~8 km), these reflectors occur in a domain that is 4 km thick.

#### 4. Discussion

In this section, we discuss the origin of the different packages of reflectors presented in the previous section and examine their possible interpretation in terms of structure and composition of the ultramafic basement. We start in the near-axis region where active deformation is documented and geological observations indicate in situ volcanism on the ultramafic seafloor, both in the axial valley floor and on the exhumed and eroded footwall near the emergence of the fault (Cannat et al., 2017).

We then examine the clusters of dipping and subhorizontal reflectors identified in the African and Antarctic plates further away from the axis, in the context of the flip-flop model proposed for this amagmatic corridor (Sauter et al., 2013). In discussing our results in the framework of this flip-flop model, we include the spatial extents of the fault systems (whose surface traces are mapped on the bathymetry as shown in Figure 1) and whose potential seismic reflectivity signatures are imaged in this study. For example, D1 represents the present-day detachment fault system characterized by an emergence (E1) and a breakaway (B1) on the surface bathymetry. Detachment fault D1, cuts through the previous detachment fault D2, displacing its emergence and breakaway into two apparent units, such that the emergence of detachment fault D2 (E2) is in the north and the breakaway (B2) is in the south of the axial domain. The previously active detachment fault D2 also cuts through the footwall of its penultimate detachment fault D3, displacing the breakaway (B3) and emergence (E3), north and south, respectively. This concept (Cannat et al., 2019; Sauter et al., 2013), in addition to explaining the dispersal of exhumed serpentinized peridotites up to 70 km across the axial domain, also provides a framework for an understanding of the reflective basement.

In our discussion, we emphasize that the constitutive crust may be heterogeneous, likely reflecting an admixture of serpentinized peridotite, variable tectonic damage, and volumetrically small magmatic intrusions. This combination of causes may explain the prevalence of the observed reflectors where the overlying ultramafic seafloor is capped by volcanics, and the sparsity of these reflectors where the seafloor is nonvolcanic. The disparity between features contemporaneous with an active fault or inherited from a previous

**Table 3**  
*Dipping Reflectors Near Axis*

Observations	Attributes	SMOO 2	SMOO 3	SMOO 33	SMOO 5
South-dipping reflectors	TWT	6.707–8.408 s	5.624–7.668 s	6.752–8.396 s	6.312–7.576 s
	Distance	1.5 to 1.7 km	–1.2 to 2.8 km	–2.6 to 1.3 km	–2.85 to 5.2 km
North-dipping reflectors	TWT	5.624–7.668 s	6.456–7.332 s	6.664–7.62 s	
	Distance	–1.4 to 6.8 km	–9.4 to 6.17 km	–8.1 to –6.45 km	
Width of the domain of south-dipping reflectors		1.15 km	1.1 km	1.82 km	0.49 km
Width of the domain of north-dipping reflectors		7.19 km	2.83 km	1.97 km	

fault system is also discussed and compared with existing geological observations, using the two-stage conceptual framework proposed for nearly amagmatic seafloor spreading in Cannat et al. (2019): (1) tectonic exhumation in the footwall of a detachment fault, and (2) further faulting, alteration, and magmatic infiltration in the hanging wall of the next detachment fault. On this basis, we propose a simplified conceptual model to explain the seismic reflection characteristics of nearly amagmatic oceanic lithosphere. Finally, we compare the results presented in this study with other observations of exhumation faulting at mid-ocean ridges, continents, and ocean-continent transition zone.

#### 4.1. Distribution, Dip, and Thickness of Active Axial Detachment Fault Damage Zone and the Seismic-Reflectivity Structure of the Footwall

The nature of the south-dipping reflectors in the axial valley indicates that the highly reflective parts are laterally offset from the inferred trace of the emergence of the active detachment fault (e.g., Figures 4b–4d). Similar reflectors were found in the narrow 3-D box (Momoh et al., 2017) as shown in Figures 6 and S8. Surrounding the very reflective parts of the south-dipping reflectors are weakly reflective events with similar dips (Figures 4c and 8). Collectively, these reflectors occur in a domain that is 490 m thick (in the eastern boundary of the investigated corridor) to 1.82 km thick (at the center of the corridor) as summarized in Table 3. The dip of these reflectors range between 45° and 50° (Figure 8). This is consistent with the ~40° dip of recent fault splays observed at the seafloor in the emergence domain (Cannat et al., 2017). Fresh volcanic patches previously interpreted as rider blocks (Reston, 2018; Sauter et al., 2013) are observed, from recent geological investigations, to be directly erupted near the emergence of the active detachment fault

D1 (Cannat et al., 2017). Therefore, magmatic injections are a third possible mechanism for the formation of the reflectors associated with D1 (in addition to tectonic damage and serpentinization).

Our preferred interpretation for these reflectors is that they result initially from fractures outlining the damage zone of the detachment fault and may serve as preferred pathways for serpentinizing fluids and magma. The reflectors can be followed consistently on all across-axis profiles discussed in this study.

These reflectors occur in the context of elevated RMBA as shown in Figure 9. RMBA reflects density variations within the crust, for example, RMBA highs indicate thinner crust or denser materials (such as weakly serpentinized to fresh peridotite) while RMBA lows represent thicker crust or lower density material such as fully serpentinized peridotites, basalts, or extensively tectonized rocks of any composition. Distinct variations occur between volcanic and smooth-seafloor terrains in the RMBA map (Cannat et al., 2006), but there is no systematic small-scale variations of RMBA values within the 64°E nearly amagmatic spreading corridor associated with local patches of volcanics, or with inferred traces of tectonic features such as the breakaway or emergence of past or active detachment faults (Figure 9). Since geological observations indicate the prevalence of serpentinized peridotite on the seafloor, moderate to high,

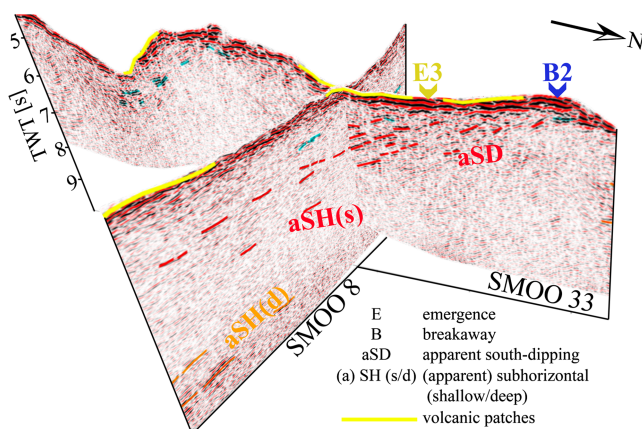


**Figure 7.** Perspective view of the intersection of apparently south-dipping reflectors (SMOO 33) and subhorizontal reflectors (SMOO 8). Both reflectors coincide in amplitudes and travel time and are therefore interpreted as traces of south-dipping reflectors. In SMOO 8, these reflectors traverse volcanic patches and melt-poor corridors, while in SMOO 33, they project to the breakaway (B2) and emergence (E3) of older detachment fault systems (D2 and D3, respectively) and sparse volcanic patches on the seafloor shown in yellow.

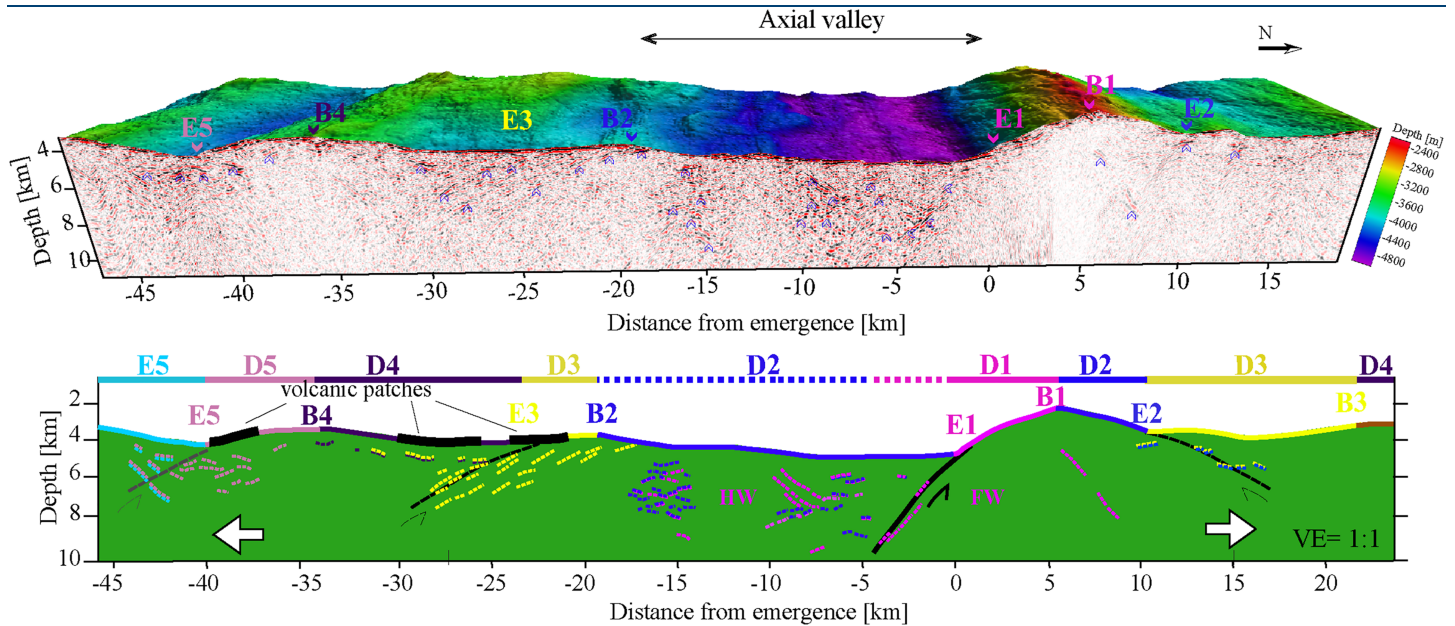


**Figure 8.** The top panel shows the depth-converted section of the combined lines (SMOO 33) using the refraction velocity model (Momoh et al., 2017) obtained on a coincident profile (Figure 1) with the bathymetry overlain. The inferred breakaway (B) and emergence (E) of present and past detachments are as indicated in Figures 1 and 4. Here, B1 and E1 are, respectively, the breakaway and emergence of detachment fault system D1, which cuts through the detachment fault D2, whose emergence (E2) is displaced further to the north as a result of exhumation and tectonic extension, and whose breakaway (B2) is displaced to the south. A selection of the most visible reflectors is indicated by arrowheads. The bottom panel shows a simplified interpretation of these reflectors. The different colors correspond to the time of activity of successive detachment faults indicated by colored lines and labels atop the figure, while the black lines at the seafloor indicate isolated volcanic patches. We interpret the reflectors as due to one, or more likely to a combination, of the following three processes: tectonic damage, intrusive magmatic bodies, or contrasts in the degree of serpentinization of the ultramafic basement. In our interpretation, we propose that the reflective character may be acquired over the lifetime of two successive axial detachment faults: damage zones created in one detachment fault can be utilized as pathways for intrusive magma or for serpentinizing fluids during the activity of the next detachment fault. For the presently active detachment fault system (D1), the footwall of the previous detachment fault system (D2) which is now the hanging wall of D1 is contemporaneously faulted with D1, with these faults also serving as pathways for magma (hence the indicated extent of D2 is shown in dashed line). The black lines in the model indicate the inferred traces of the active and inactive (dashed) detachment faults. If correct, our interpretation suggests that the shallow parts of detachment fault systems (<5 km) are steep (45–55°) at an early stage of the fault's activity (represented by the presently active axial detachment), and rotate to a shallower-dipping angle (25°) after about 16 km of horizontal displacement (estimated for detachment fault D3; Cannat et al., 2019).

the RMBA values near the emergence of active and inactive detachment faults could be interpreted as an indication that extensive serpentinization (i.e., lower densities) does not extend over a thick domain next to these faults at infracrustal (>5 km) depth. Figure 10 shows that shipboard free-air gravity data are not very sensitive to variations in density occurring at depths greater than a few km below the seafloor. In this, we compare measured free-air gravity anomalies (FAA) and 2-D forward gravity models with thick serpentinized domains (i.e., damaged zones) along the presently active axial detachment fault to a depth of 25 km. Specifically, Figure 10 shows that the available gravity data do not rule out thin (<3 km) domains of partially serpentinized mantle along these faults extending to substantial depths (up to 25 km).

While the fault damage zones at mid-ocean ridge systems documented in the geological literature are narrow (<400 m), for example, (Hayman & Karson, 2007), our results confirm findings of Momoh et al. (2017) and indicate that a thicker damage zone is likely even for short-offset faults (present offset at young D1 axial detachment fault is estimated as <4 km; Cannat et al., 2019). Following on the discussion in Momoh et al. (2017), we propose that this young yet thick damage zone may have formed in three ways: (1) due to distributed simultaneous deformation over a thick domain, (2) as a finite damage zone due to strain localizing on a succession of subparallel individual fault segments, or (3) by a combination of both styles. Numerical experiments incorporating the proportion of plate divergence taken by magmatic diking versus tectonic extension (the *M* factor of Buck et al., 2005) predict that when the proportion of melt supply is <50%, the fault system tends to migrate toward the hanging wall. As proposed by Momoh et al. (2017), this migration may play a role in generating a thicker damage zone.

Broad fault damage zones have been documented next to onland major faults, for example, at the Calico strike-slip fault system, reduction in compressional wave velocity and shear moduli interpreted as due to

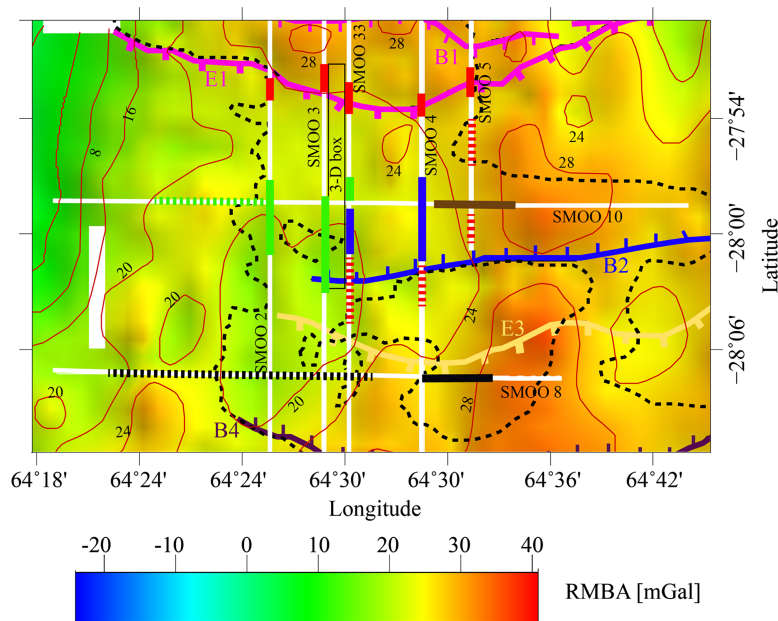


**Figure 9.** Distribution of the main groups of identified reflectors on a Residual Mantle Bouguer Anomaly (RMBA) map calculated from gravity data collected in the area (Cannat et al., 2006). The inferred breakaway (B) and the emergence (E) of present and past detachment faults, and the limits of volcanic seafloor areas (black dashed lines) are indicated as in Figure 1. The main groups of reflectors are projected along the traces of corresponding seismic profiles (white lines). RMBA are distinctly lower in the volcanic domain to the west (western end of SMOO 10), and distinctly higher in the eastern part of the surveyed area (SMOO 5 and the eastern ends of SMOO 8 and SMOO 10). Within the investigated domain, RMBA variations do not appear to correlate with the main tectonic features (emergence, breakaway, and limits of patches of volcanic seafloor). This indicates that these features are not associated with systematic changes in crustal density and/or thickness. Specifically, we note that the emergence region of past and present axial detachment faults are not associated with lower RMBA values as would be the case if deep-seated serpentinization was extensive in these regions.

finite damage arising from historical ruptures is observed in a zone that is 1.5 km wide (Cochran et al., 2009). Another example of a broad fault damage zone is the Alpine fault in New Zealand which exhumed rocks from depths of ~35 km, and is characterized by a 1-2 km fractured domain (Little et al., 2005; Townend et al., 2017; Williams et al., 2018). Other laboratory, field, and model-based studies predict that zones of mechanical damage around a fault are <1 km thick in terrestrial systems for fault offsets of 10 km (Faulkner et al., 2011; Savage & Brodsky, 2011). These observations point to significant differences in the magnitudes of damage around different fault systems. This variability may be due to differences in tectonic settings (extensional versus strike-slip or compressional), and in deformation mechanisms (Faulkner et al., 2010).

Within the footwall of active detachment fault D1, the reflector dipping north 45° (Figure 8) may be due to fractures arising from footwall bending during tectonic uplift by the active detachment fault. Features of this nature have been attributed to reverse faulting due to compression-induced cracks from footwall bending, for example, at the 13°20'N OCC, earthquake hypocenters outline steeply dipping events (from 3 to 7 km below the seafloor) of a mature detachment fault system (Parnell-Turner et al., 2017); while at the Trans-Atlantic Geotraverse, they are traced on earthquake hypocenters from 5 to 8 km below the seafloor (deMartin et al., 2007). Footwall bending-induced cracks which can be fluid-filled or act as feeder systems for magma emplacement on the seafloor may also give rise to this type of reflection within the predominantly ultramafic basement. Our proposed interpretation is that the reflectors are indicative of accommodation faults within the footwall of the active axial detachment fault, which accommodate some of the internal

deformation when the footwall bends during exhumation. Depending on the proximity of these accommodation faults to the magmatic systems and their connection to the surface, they may also serve as a part of the magmatic plumbing system during the lifetime of the detachment fault. Further to the north, the reflectors parallel to the seafloor may reflect traces of the extent of damage in the footwall (serpentinization) or may reflect boundaries between intrusive magmatic sills and partially serpentinized peridotite of the penultimate detachment fault system (D2). There is no evidence for isolated volcanic edifices in the north, which may explain why the reflectors are sparse there.

#### 4.2. Architecture of the Hanging Wall of the Axial Detachment Fault (Near-Axis Portion of the Antarctic Plate)

The near-axis portion of the hanging wall of the active detachment fault shows two sets of reflectors: reflectors that are north-dipping and subhorizontal reflectors. The north-dipping reflectors, also observed in the 3-D box (Momoh et al., 2017), are apparent on the two bounding lines (SMOO 2 and SMOO 3) on the west (Figures 4a and 4b), and SMOO 33 in the east of the box (Figure 4c). These north-dipping reflectors are shallow-dipping toward the west of the survey area as shown in Figure 4a and coincide with the east-dipping reflectors observed on the crossing profile (SMOO 10) as shown in Figures 5b and 6. On the RMBA (Figure 9), these north-dipping reflectors project to areas with moderate RMBAs.

Considering that the north-dipping reflectors moderately offset the seafloor (<200 m) in the axial valley and project to areas with moderate RMBA, we align with our previous interpretation that they are associated with recent conjugate faults formed in the hanging wall simultaneously serving as magmatic conduits

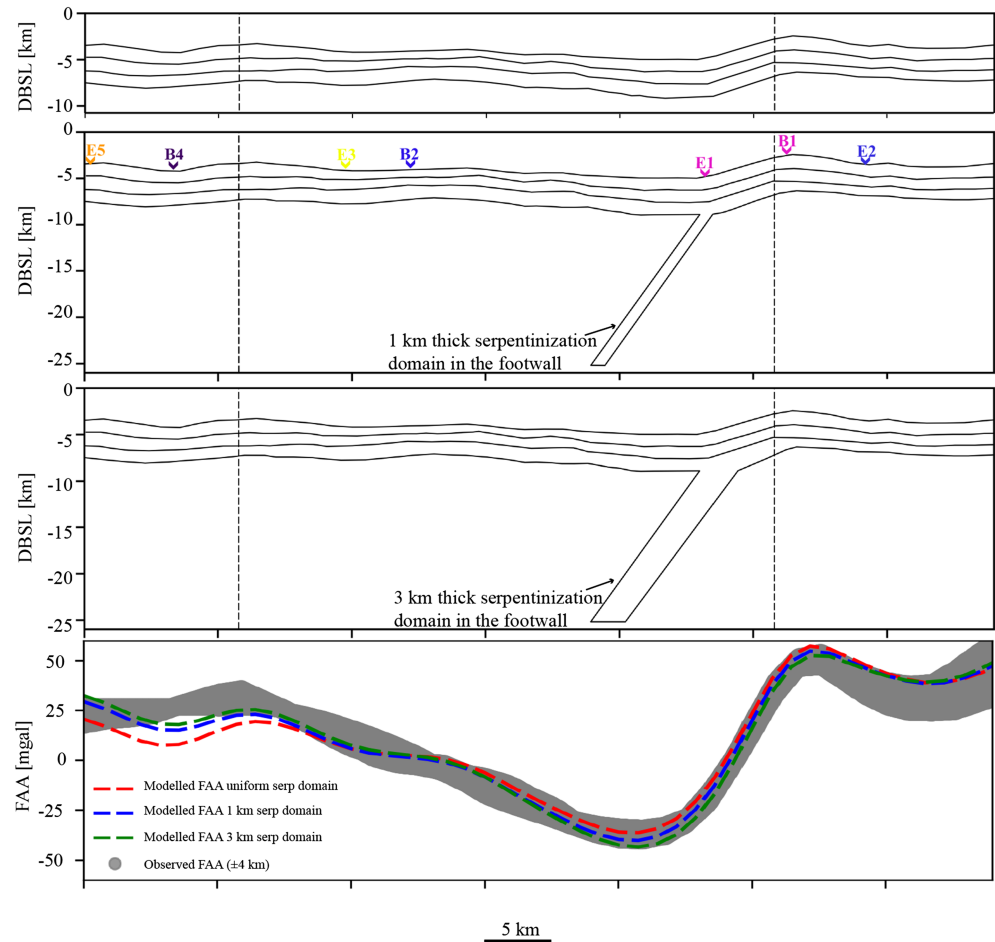


**Figure 10.** Comparison of the envelop of observed FAA data within a domain of  $\pm 4$  km from SMOO 33 with 2-D forward modeled FAA data for two geometries examining the width and depth of the serpentinization domain. The density blocks have been computed from the compressional wave velocity model using Gardner's law (Gardner et al., 1974). The vertical dashed lines indicate the limits of the  $P$  wave velocity model from a collocated wide-angle refraction profile from which the densities are estimated.

onto the seafloor (Momoh et al., 2017). This is further corroborated by the coinciding east dipping reflectors on SMOO 10 which project to the volcanic seafloor (Figures 5b and 6). One of the north-dipping reflectors from the 3-D box underlies an isolated patch of volcanic seafloor (Figures 6 and S7), a hint of this occurrence is between 13 and 15 km south of the inferred emergence on SMOO 3 (Figure 4b). The contemporaneity of the features interpreted as faults in the hanging wall of the active detachment fault system with the active detachment fault D1, suggests that the exhumed footwall of the previous detachment fault system (D2) which is presently the hanging wall of the active detachment fault system (D1) is pervasively faulted. Therefore, tectonic damage zones of D2 may either be utilized for magma emplacement or “overprinted” by the recent hanging wall normal faults. The subhorizontal reflectors may be due to boundaries between magmatic intrusions (sills) dispersed within the ultramafic basement in the current detachment fault cycle (D1), or between parts of the ultramafic basement that are highly serpentinized and those that are partially serpentinized and fresher peridotite, or a combination of both; or magma-filled damaged zones inherited from detachment fault system D2. If the conjugate-fault-magmatic-conduit/sill interpretation is correct, then it follows that the magmatic conduits are found in only a portion of the ultramafic basement. In conclusion, we interpret the seismic reflectivity structure of this ultramafic basement in terms of fault damage, serpentinization and incipient magmatism incurred in the framework of its two-stage evolution (Cannat et al., 2019) during (1) its exhumation in the footwall of an earlier detachment fault, and (2) its evolution as part of the hanging wall of the next detachment fault (Cannat et al., 2019).

### 4.3. Structure of the Ultramafic Basement in the Antarctic Plate

Away from the axial valley, a package of south-dipping reflectors strongly visible between 18 and 27.5 km south of the inferred emergence of detachment fault D3, with traces of this event in SMOO 4 between 20 and 27.5 km south of the inferred emergence (Figure S4b) is observed between the breakaway (B2) of detachment fault 2 (D2) and the emergence (E3) of detachment fault 3 (D3). On both profiles, these reflectors project to volcanic patches on the ultramafic seafloor (Figures 4, 7, and S4) corresponding to lower RMBA values (Figure 9). On SMOO 33 (Figure 4c), at the inferred emergence of detachment fault D2 (E2), we can observe an isolated reflector with the same apparent dip. We now examine two hypotheses for the formation of the reflectors presented above and propose that they may actually form by a combination of the two.

The first hypothesis is that they are associated with the damage zone of detachment fault 3 (D3). This is analogous to the present-day detachment fault characterized by reflectors in the footwall beneath the emergence of the active fault, but the former reflectors are less steep ( $25^\circ$  vs.  $50\text{--}55^\circ$ ).

We propose that these lower angles may result from the more significant footwall rotation incurred in the detachment fault (D3) system as it terminated after an estimated 16 km of horizontal displacement (Cannat et al., 2019). Compared to the present-day detachment fault damage zone, which has so far accommodated  $\sim 4$  km of horizontal displacement only (Cannat et al., 2019), and assuming a linear relationship between horizontal offsets and emergence angles, then the flexural rate in the shallow footwall of these detachment faults is  $\sim 2.5^\circ/\text{km}$  of fault displacement. This is significantly less than the flexural rate that could be estimated (assuming a similar initial dip of the fault at shallow depth) for the shallow footwall of MAR corrugated OCCs: the emergence angle of the  $13^\circ\text{N}$  active detachment fault is less than  $10^\circ$  (Smith et al., 2006) for a total horizontal displacement of  $\sim 12$  km (MacLeod et al., 2009).

The second hypothesis is that these south-dipping reflectors are signatures of magmatic channels feeding the nearby volcanic patches at the seafloor. This may account for the extensive volcanic patches that are observed both in the hanging wall and footwall of D3 (Sauter et al., 2013). This mechanism is the same proposed above to explain the subhorizontal reflectors observed in the hanging wall of the active detachment fault D1. The lack of continuity of the south dipping and subhorizontal reflectors, consequently the heterogeneity of the crust, may be explained by the lack of continuity of the magmatic conduits and lenses, suggesting that the magma present is localized to a small area.

Our preferred interpretation is that the damage zones formed during the activity of detachment fault D3 may subsequently have served as feeder systems for magma (combination of the two hypotheses presented above).

The deepest cluster of bright reflectors imaged at depth  $\sim 9.3$  km on the along-axis profile (SMOO 8) 33 km south of the axial domain is  $\sim 4$  km thick and extends  $\sim 6$  km in the along-axis direction (Figure 5b). This cluster of reflectors is located in the footwall of detachment fault D3,  $\sim 1.5$  km from its inferred emergence (E3). It is observed beneath a large volcanic patch in the ultramafic corridor (Figure 9). This cluster of reflectors may be an indicator of localized magmatic infiltrations and lenses within the deep lithosphere. Such infiltrations have been documented on dredged samples of infiltrated peridotites from the same area by Paquet et al. (2016), leading to a conceptual model for the nearly amagmatic section of the easternmost Southwest Indian Ridge in which magmatic lenses and conduits are distributed at various depths in the entire axial lithosphere (Cannat et al., 2019).

Based on these results and on the results we have presented here, we propose that the seismic reflectivity signature of the nearly amagmatic oceanic lithosphere forms in the context of successive flip-flop detachment fault systems that cuts through the entire brittle lithosphere. While we have only imaged the uppermost 5 km of the fault system (as shown in Figure 8), we propose a steepening downward of the fault system (as shown in dashed line for the D3 case with the imaged part shown in bold line), rooting into a mostly melt-starved, but locally infiltrated ductile mantle (Figure 11). The rooting depth is inferred from microseismic activities recorded near  $66^\circ\text{E}$  (Schlindwein & Schmid, 2016). The package of deep (9.3–13 km) and apparently subhorizontal reflectors imaged along profile SMOO 8 (Figure 5) could provide us with an estimate of the spatial extent of magmatic infiltration domains in the brittle lithosphere. Our interpretation is that this package represents an ancient infiltration domain, now cooled and crystallized, that formed

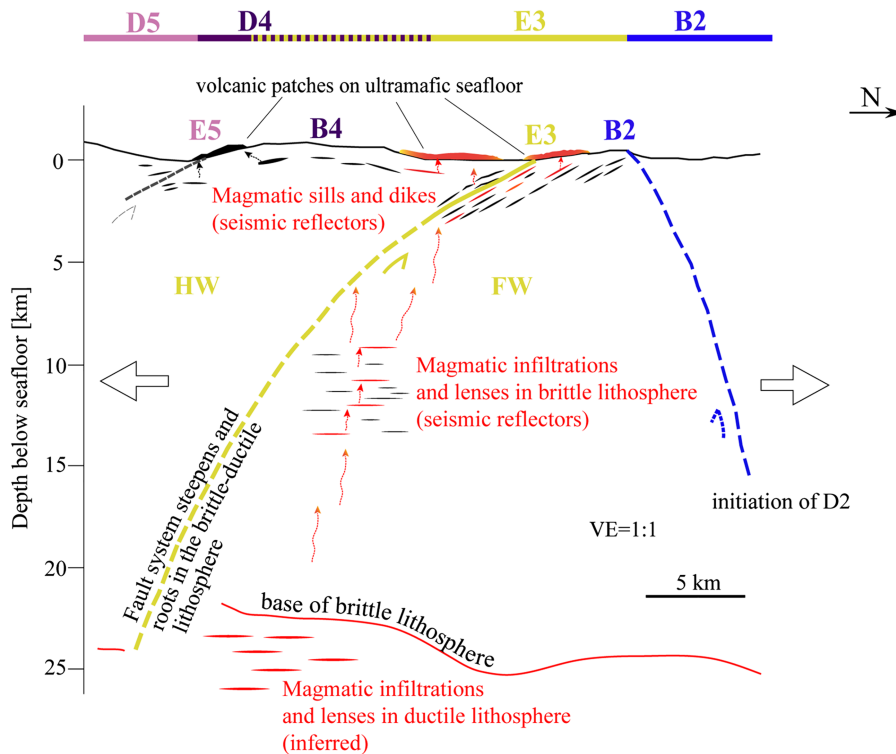


**Figure 11.** Conceptual model for a mature stage of detachment fault system D3, at the time of initiation of detachment fault system D2 (geometry is inferred from the presently active detachment fault D1). The part of the D3 fault system we have imaged is shown in solid line, while the part of the fault system shown in dashed line is inferred. The imaged part of the D3 fault system dips 25° in the uppermost basement (from our interpretation of the package of dipping reflectors in SMOO 4 and SMOO 33) and we propose it steepens, rooting at a localized magmatically infiltrated domain near the brittle-ductile transition zone. The depth to this zone is inferred from the depth of earthquake recorded in the 65°25'E region of the SWIR (Schlindwein & Schmid, 2016). Outer packages of shallow-dipping to subhorizontal reflectors identified in SMOO 33 (Figure 8) are proposed to have formed first as damage zones in the footwall of detachment fault D4, then as pathways for magmatic intrusions in the hanging wall of D3. The deep package of reflectors identified over an along-axis distance of 4 km (with the top located at least 9.3 km) in SMOO 8 (Figures 5 and 8) is interpreted as due to magmatic infiltrations in the lower brittle lithosphere which would correspond to samples of magmatically impregnated peridotites (Paquet et al., 2016). Deeper magmatic lenses are inferred in the ductile lithosphere. This localized system may serve as a source for the volcanic patches observed at the seafloor.

In this section, we first compare our observations with seismic images of detachment fault systems at the distal parts of ocean-continent transition (OCT) zones, packages of dipping reflectors beneath OCT ridges, and subhorizontal reflectors. In the OCT settings, active processes are long past and geological interpretation of the imaged reflectors is made more difficult due to more extensive sediment cover. On the other hand, thick sediment cover allows for good signal penetration and better imaging of reflectors, be they caused by faults, unconformities or magmatic sills and dikes.

The prominent “S” reflector observed in the Deep Galicia Margin (Boillot et al., 1980; Dean et al., 2015) is interpreted as a concave upward detachment fault, which exhumed subcontinental mantle (Boillot et al., 1980; Reston, Ruo et al., 1996). Image-enhanced 3-D seismic data show that the surface of this reflector is corrugated (Schuba et al., 2018). It is proposed to have slipped at 20° (Reston et al., 1996). Overlying this reflector are a suite of high-angle normal faults terminating on the reflector (Reston et al., 1996; Davy et al., 2017).

Compared to the detachment fault interpretation we have discussed at the nearly amagmatic easternmost SWIR, the domain of exhumed subcontinental mantle of magma-poor OCT zones such as the

during the period of activity of detachment fault D3. This locally infiltrated domain was probably fed by magmatic sources located deeper, beyond the limits of our imaging capabilities. Using subvertical dikes and the detachment fault system damaged zones, some of the ascending magma may be extracted and form the isolated volcanic patches shown in Figure 11. Our conceptual model (Figure 11) proposed for the time of termination of detachment fault D3, combines the two hypotheses presented above to account for the observed reflectors: damage, alteration, and incipient magmatism in the footwall of detachment fault D4, is followed by further faulting and magmatic infiltrations in the footwall and hanging wall of detachment fault D3. Some of the imaged reflectors, for example between emergence (E5) of detachment fault system D5 and the emergence (E3) of detachment fault system D3 follow the seafloor topography. This suggests that they may have been parallel to the exhumed portion of detachment fault D4, outlining a magma-infiltrated damage zone formed either during D4 detachment fault cycle or during D3 detachment fault cycle. We thus propose again that magmatic intrusions, even though volumetrically small, cause some parts of the basement to show reflective signatures. The initiation of the subsequent detachment fault D2 is inferred to be initially steep (shown in dashed line).

#### 4.4. Comparison With Seismic Observations at Other Detachment Fault Systems at Mid-Ocean Ridges and Ocean-Continent Transition Zones

The study presented in this paper provides insights on the seismic reflectivity structure of the oceanic lithosphere formed in nearly amagmatic conditions at an ultraslow spreading mid-ocean ridge.

Australia-Antarctica and West Iberia margins has been explained by slip along a single detachment fault with the passive addition of magma along the fault (Gillard, Manatschal, & Autin, 2016); while at the proto-oceanic domain in the most distal part of the margins (the transition from the zone of exhumed continental mantle to unambiguous oceanic crust), short-offset flip-flop detachment faults are proposed to develop at the final stages of rifting (Gillard et al., 2015; Gillard, Autin, & Manatschal, 2016; Reston & McDermott, 2011). In the zone of exhumed continental mantle, locally reflective features above detachment fault surfaces have been attributed to localized magmatic extrusives where short-offset normal faults (overlying the main detachment fault) can serve as feeder systems for magma (Gillard et al., 2015).

The exhumed detachment fault surface at the Galicia margins is long inactive and mostly inaccessible. The geology of this magma-poor distal OCT domain is primarily inferred from ocean drilling. The interpretations we propose for seismic reflectors formed in the context of nearly amagmatic oceanic accretion are, by contrast, based on robust geological evidence for the geometry and chronology of recent and active faults, and for the interplays of these faults with incipient magmatism. Reflective features in a magma-poor basement may be acquired from a combined tectonic and magmatic activity where damaged zones become sites for magma emplacement. Also, our interpretation of short-offset normal faults playing a dual role of accommodating some of the deformation in the hanging wall and serving as magmatic conduits channeling some of the magma vertically and laterally to the seafloor can be used to examine the interpretation of some of these reflectors in the OCT domains.

A study of three seismic transects near the Gulf of Aden, south of Oman in three adjacent segments encompassed the distal margin of the OCT and showed variability in rifted margin geometry, crustal thickness, and magmatism over short distances (Leroy et al., 2010). For example, while the role of exhumation faulting is thought to be common even in the magma-rich segment investigated, the seismic signatures for this are apparently elusive, yet the presence of dipping reflectors extending ~10 km southward beneath the foot of a volcano has been attributed to magmatic underplating, a volcano-sedimentary wedge or lava flows or sills which intruded under the OCT ridge (Autin et al., 2010; Leroy et al., 2010). While these features are mostly linked to a volcanic origin, their emplacement history, that is, whether they arose during postrift magmatic activity or they were coeval with OCT ridge formation by detachment faulting are subject to uncertainties. This disparity can be further assessed using some of the ideas we have discussed here, because we observed reflectors beneath the inferred emergence of an inactive detachment fault projecting to seafloor where volcanic patches are apparent.

The emplacement history of the volcanics in the OCT ridge near the Gulf of Aden giving rise to the reflectors can be assessed in the context of localized magmatic activity spread throughout the lifetime of exhumation faulting and not necessarily due to a high magma influx near the end of rifting. Although our study did not focus on volcanic terrains, we note that the dipping reflectors are prevalent where the overlying seafloor is covered by volcanic patches, no matter how small. Therefore, if exhumation tectonics do occur in magmatically rich distal margins, the magmatic extrusives may exploit the detachment fault system for emplacement which may be the reason why these features are reflective in the magma-rich margin segment yet less so in the magma-poor segment as we also found in our results.

The subhorizontal reflectors of variable width have also been reported in the zone of exhumed continental mantle in the Iberia-Newfoundland margin and Australian-Antarctic margin (Gillard, Autin, & Manatschal, 2016; Gillard, Manatschal, & Autin, 2016; Peron-Pinvidic et al., 2010). These reflectors are normally interpreted in the context of passive addition of magma along the footwall of an active detachment fault; or when the system is magmatically driven, as arising from a high influx of magma and sill injections which can be locally reflective in a predominantly ultramafic basement (Gillard, Manatschal, & Autin, 2016). The study which we have presented here can be used to assess the conditions of the ultramafic basement at final stages of rifting before seafloor spreading in the context of the dipping and subhorizontal reflectors which we have related to detachment faulting and the distribution of localized magmatic infiltrations in a two phase evolutionary sequence in the hanging wall and footwall of the detachment fault.

Seismic reflection imaging of active detachment fault systems at mid-ocean ridges, has by contrast, been mostly elusive due to very little sediment cover and rough seafloor leading to scattering of seismic waves and poor signal penetration (Canales et al., 2004). Despite these limitations, and in addition to the expedition that acquired the data reported here, recent seismic reflection investigations of, for example, the Rainbow

Massif located at a non-transform discontinuity of the Mid-Atlantic Ridge, imaged dipping reflectors associated with strong lateral velocity variations which are attributed to alteration contacts, faulting or lithologic boundaries associated with a detachment fault inferred to have terminated (Canales et al., 2017). This study also imaged prominent packages of subhorizontal reflectors in the crust and uppermost mantle, interpreted as magmatic sills, some of which are probably not fully crystallized and provide heat to the active Rainbow black smokers (Canales et al., 2017). This area of the MAR is significantly more magmatically active than our eastern SWIR study area, yet there are similarities between these inferred sills and the less abundant and more localized subhorizontal reflectors which we also interpret as sills.

## 5. Conclusions

The easternmost Southwest Indian Ridge near 64°E of longitude, represents a nearly amagmatic end-member in the global mid-ocean ridge system. With corridors of seafloor exhibiting outcrops of serpentized peridotites on both diverging plates between more magmatically robust terranes, it affords a unique opportunity to investigate the nature of the geophysical crust formed in this nearly amagmatic context and to test the tectonic hypothesis proposed for this end-member mode of seafloor spreading. These include flip-flop faulting, extensive alteration and incipient magmatism. The SISMOSMOOTH experiment provided seismic reflection data which we have analyzed and discussed in this study, following an earlier paper that focused on a narrow, on-axis quasi-3-D seismic reflection acquisition (Momoh et al., 2017). Our new results lead to the following main conclusions:

1. Damage zones characterize the active detachment fault system with dip  $\sim 50^\circ$  in the uppermost 5 km. A mature detachment fault system is associated with shallower dips ( $\sim 25^\circ$ ) which may be the result of footwall rotation after developing  $\sim 16$  km of horizontal offset.
2. Reflectors in the ultramafic basement can be explained in a two-phase evolutionary sequence that takes place in two detachment fault cycles (Cannat et al., 2019). Phase one involves tectonic damage, serpentization, footwall flexure, and incipient magmatism in the footwall of one detachment fault. Phase two involves further faulting, alteration, and magmatic infiltration in the hanging wall of the next detachment fault. More highly reflective basement domains may likely be linked to more abundant magmatic rocks in the ultramafic basement.
3. The geophysically defined crust is heterogeneous reflecting a tectonically damaged and serpentized ultramafic basement with localized intrusive magmatic bodies.

## Acknowledgments

We thank the Flotte Oceanographique Francaise (FOF) for funding the SISMOSMOOTH cruise and Institut Polaire Francais Paul Emile Victor (IPEV) for the cruise aboard the French research vessel *Marion Dufresne* (technical team led by Helene Leau). CNRS-INSU program Tellus provided support for the cruise and postcruise research. The work was supported by ANR projects Rift2Ridge (NT09-48546) and RidgeFactory (ANR-18-CE01-0002-01). We thank Captain Thierry Dudouit (CMO-CGM) and the crew of the R/V *Marion-Dufresne*: Erwan Nedelec and Jean-Charles Guedes (Genavir) for the seismic deployment. We thank Satish Singh for suggesting we combine three seismic lines. We also thank Manon Bickert for sharing her numerical models and for geological discussions. Navigation (.P190) data generated are available at <https://campagnes.flotteoceanographique.fr/campagnes/14003300/>, while the raw and processed seismic data shall be made available upon demand at this site (<https://campagnes.flotteoceanographique.fr/campagnes/14003300/>). This is IPGP contribution number 4076.

## References

- Andreani, M., Mevel, C., Boullier, A. -M., & Escartin, J. (2007). Dynamic control on serpentine crystallization in veins: Constraints on hydration processes in oceanic peridotites. *Geochemistry, Geophysics, Geosystems*, 8, Q02012. <https://doi.org/10.1029/2006GC001373>
- Autin, J., Leroy, S., Beslier, M. O., d'Acremont, E., Razin, P., Ribodetti, A., et al. (2010). Continental break-up history of a deep magma-poor margin based on seismic reflection data (northeastern Gulf of Aden margin, offshore Oman). *Geophysical Journal International*, 180(2), 501–519. <https://doi.org/10.1111/j.1365-246X.2009.04424.x>
- Blackman, D. K., Karson, J. A., Kelley, D. S., Cann, J. R., Früh-Green, G. L., Gee, J. S., et al. (2002). Geology of the Atlantis Massif (Mid-Atlantic Ridge, 30°N): Implications for the evolution of an ultramafic oceanic core complex. *Marine Geophysical Researches*, 23(5/6), 443–469. <https://doi.org/10.1023/B:MARI.0000018232.14085.75>
- Boillot, G., Grimaud, S., Mauffret, A., Mougnot, D., Kornprobst, J., Mergoil-Daniel, J., & Torrent, G. (1980). Ocean-continent boundary off the Iberian margin: A serpentinized diapir west of the Galicia Bank. *Earth and Planetary Science Letters*, 48(1), 23–34. [https://doi.org/10.1016/0012-821X\(80\)90166-1](https://doi.org/10.1016/0012-821X(80)90166-1)
- Bolondi, G., Loinger, E., & Rocca, F. (1982). Offset continuation of seismic sections. *Geophysical Prospecting*, 30(6), 813828. <https://doi.org/10.1111/j.1365-2478.1982.tb01340.x>
- Buck, W. R., Lavier, L. L., & Poliakov, A. N. (2005). Modes of faulting at mid-ocean ridges. *Nature*, 434(7034), 719–723. <https://doi.org/10.1038/nature03358>
- Cabrera, J., & Levy, S. (1989). Shot dip moveout with logarithmic transformations. *Geophysics*, 54(8), 1038–1041. <https://doi.org/10.1190/1.1442729>
- Canales, J. P., Dunn, R. A., Arai, R., & Sohn, R. A. (2017). Seismic imaging of magma sills beneath an ultramafic-hosted hydrothermal system. *Geology*, 45(5), 451–454. <https://doi.org/10.1130/G38795.1>
- Canales, J. P., Tucholke, B., & Collins, J. (2004). Seismic reflection imaging of an oceanic detachment fault: Atlantis megamullion (Mid-Atlantic Ridge, 30°N). *Earth and Planetary Science Letters*, 222(2), 543–560. <https://doi.org/10.1016/j.epsl.2004.02.023>
- Canales, J. P., Tucholke, B. E., Xu, M., Collins, J. A., & DuBois, D. L. (2008). Seismic evidence for large-scale compositional heterogeneity of oceanic core complexes. *Geochemistry, Geophysics, Geosystems*, 9, Q08002. <https://doi.org/10.1029/2008GC002009>
- Cann, J., Blackman, D., Smith, D., McAllister, E., Janssen, B., Mello, S., & Escartin, J. (1997). Corrugated slip surfaces formed at ridge-transform intersections on the Mid-Atlantic Ridge. *Nature*, 385(6614), 329–332. <https://doi.org/10.1038/385329a0>

- Cannat, M. (1993). Emplacement of mantle rocks in the seafloor at mid-ocean ridges. *Journal of Geophysical Research*, 98(B3), 4163–4172. <https://doi.org/10.1029/92JB02221>
- Cannat, M., Agrinier, P., Bickert, M., Brunelli, D., Hamelin, C., Lecoeuvre, A., et al. (2017). Mid-ocean ridge processes at very low melt supply: Submersible exploration of smooth ultramafic seafloor at the Southwest Indian Ridge, 64°E. In AGU Fall Meeting Abstracts.
- Cannat, M., Fontaine, F., & Escartin, J. (2010). Serpentinization and associated hydrogen and methane fluxes at slow spreading ridges. In *Diversity of hydrothermal systems on slow spreading ocean ridges* (pp. 241–264). Washington: American Geophysical Union. <https://doi.org/10.1029/2008GM000760>
- Cannat, M., Mevel, C., Maia, M., Deplus, C., Durand, C., Gente, P., et al. (1995). Thin crust, ultramafic exposures, and rugged faulting patterns at the Mid-Atlantic Ridge (22–24°N). *Geology*, 23(1), 49. [https://doi.org/10.1130/0091-7613\(1995\)0230049:TCUEAR2.3.CO;2](https://doi.org/10.1130/0091-7613(1995)0230049:TCUEAR2.3.CO;2)
- Cannat, M., Rommevaux-Jestin, C., Sauter, D., Deplus, C., & Mendel, V. (1999). Formation of the axial relief at the very slow spreading Southwest Indian Ridge (49° to 69°E). *Journal of Geophysical Research*, 104(B10), 22,825–22,843. <https://doi.org/10.1029/1999JB900195>
- Cannat, M., Sauter, D., Bezos, A., Meyzen, C., Humler, E., & Le Rigoleur, M. (2008). Spreading rate, spreading obliquity, and melt supply at the ultraslow spreading South-west Indian Ridge. *Geochemistry, Geophysics, Geosystems*, 9, Q04002. <https://doi.org/10.1029/2007GC001676>
- Cannat, M., Sauter, D., Lavier, L., Bickert, M., Momoh, E., & Leroy, S. (2019). On spreading modes and magma supply at slow and ultraslow mid-ocean ridge. *Earth and Planetary Science Letters*, 519, 223–233. <https://doi.org/10.1016/j.epsl.2019.05.012>
- Cannat, M., Sauter, D., Mendel, V., Ruellan, E., Okino, K., Escartin, J., & Baala, M. (2006). Modes of seafloor generation at a melt-poor ultraslow-spreading ridge. *Geology*, 34(7), 605–608. <https://doi.org/10.1130/G22486.1>
- Claerbout, J. F., & Johnson, A. G. (1971). Extrapolation of time-dependent waveforms along their path of propagation. *Geophysical Journal International*, 26(1-4), 285–293. <https://doi.org/10.1111/j.1365-246X.1971.tb03402.x>
- Cochran, E. S., Li, Y.-G., Shearer, P. M., Barbot, S., Fialko, Y., & Vidale, J. E. (2009). Seismic and geodetic evidence for extensive, long-lived fault damage zones. *Geology*, 37(4), 315–318. <https://doi.org/10.1130/G25306A.1>
- Davy, R. G., Morgan, J. V., Minshull, T. A., Bayrakci, G., Bull, J. M., Klaeschen, D., et al. (2017). Resolving the fine-scale velocity structure of continental hyperextension at the Deep Galicia Margin using full-waveform inversion. *Geophysical Journal International*, 212(1), 244–263. <https://doi.org/10.1093/gji/ggx415>
- Dean, S. L., Sawyer, D. S., & Morgan, J. K. (2015). Galicia Bank ocean–continent transition zone: New seismic reflection constraints. *Earth and Planetary Science Letters*, 413, 197–207. <https://doi.org/10.1016/j.epsl.2014.12.045>
- deMartin, B. J., Sohn, R. A., Pablo Canales, J., & Humphris, S. E. (2007). Kinematics and geometry of active detachment faulting beneath the Trans-Atlantic Geotraverse (TAG) hydrothermal field on the Mid-Atlantic Ridge. *Geology*, 35(8), 711–714. <https://doi.org/10.1130/G23718A.1>
- Deregowski, S., & Rocca, F. (1981). Geometrical optics and wave theory of constant offset sections in layered media. *Geophysical Prospecting*, 29(3), 374–406. <https://doi.org/10.1111/j.1365-2478.1981.tb01020.x>
- Dick, H. J., Lin, J., & Schouten, H. (2003). An ultraslow-spreading class of ocean ridge. *Nature*, 426(6965), 405–412. <https://doi.org/10.1038/nature02128>
- Dick, H. J., Tivey, M. A., & Tucholke, B. E. (2008). Plutonic foundation of a slow-spreading ridge segment: Oceanic core complex at Kane Megamullion, 23°30'N, 45°20'W. *Geochemistry, Geophysics, Geosystems*, 9, Q05014. <https://doi.org/10.1029/2007GC001645>
- Dunn, R. A., Arai, R., Eason, D. E., Canales, J. P., & Sohn, R. A. (2017). Three-dimensional seismic structure of the Mid-Atlantic Ridge: An investigation of tectonic, magmatic, and hydrothermal processes in the Rainbow area. *Journal of Geophysical Research: Solid Earth*, 122, 9580–9602. <https://doi.org/10.1002/2017JB015051>
- Escartin, J., Smith, D. K., Cann, J., Schouten, H., Langmuir, C. H., & Escrig, S. (2008). Central role of detachment faults in accretion of slow-spreading oceanic lithosphere. *Nature*, 455(7214), 790–794. <https://doi.org/10.1038/nature07333>
- Faulkner, D., Mitchell, T., Jensen, E., & Cembrano, J. (2011). Scaling of fault damage zones with displacement and the implications for fault growth processes. *Journal of Geophysical Research*, 116, B05403. <https://doi.org/10.1029/2010JB007788>
- Faulkner, D. R., Jackson, C. A. L., Lunn, R. J., Schlische, R. W., Shipton, Z. K., Wibberley, C. A. J., & Withjack, M. O. (2010). A review of recent developments concerning the structure, mechanics and fluid flow properties of fault zones. *Journal of Structural Geology*, 32(11), 1557–1575. <https://doi.org/10.1016/j.jsg.2010.06.009>
- Fruh-Green, G. L., Connolly, J. A., Plas, A., Kelley, D. S., & Grobety, B. (2004). Serpentinization of oceanic peridotites: Implications for geochemical cycles and biological activity. *The seafloor biosphere at mid-ocean ridges*, 144, 119–136. <https://doi.org/10.1029/144GM08>
- Garces, M., & Gee, J. S. (2007). Paleomagnetic evidence of large footwall rotations associated with low-angle faults at the Mid-Atlantic Ridge. *Geology*, 35(3), 279–282. <https://doi.org/10.1130/G23165A.1>
- Gardner, G. H. F., Gardner, L. W., & Gregory, A. R. (1974). Formation velocity and density- the diagnostic basics for stratigraphic traps. *Geophysics*, 39(6), 770–780. <https://doi.org/10.1190/1.440465>
- Gillard, M., Autin, J., & Manatschal, G. (2016). Fault systems at hyper-extended rifted margins and embryonic oceanic crust: Structural style, evolution and relation to magma. *Marine and Petroleum Geology*, 76, 5167. <https://doi.org/10.1016/j.marpetgeo.2016.05.013>
- Gillard, M., Autin, J., Manatschal, G., Sauter, D., Munschy, M., & Schaming, M. (2015). Tectonomagmatic evolution of the final stages of rifting along the deep conjugate Australian-Antarctic magma-poor rifted margins: Constraints from seismic observations. *Tectonics*, 34, 753–783. <https://doi.org/10.1002/2015TC003850>
- Gillard, M., Manatschal, G., & Autin, J. (2016). How can asymmetric detachment faults generate symmetric ocean continent transitions? *Terra Nova*, 28(1), 27–34. <https://doi.org/10.1111/ter.12183>
- Hale, D. (1984). Dip-moveout by Fourier transform. *Geophysics*, 49(6), 741–757. <https://doi.org/10.1190/1.1441702>
- Hayman, N. W., & Karson, J. A. (2007). Faults and damage zones in fast-spread crust exposed on the north wall of the Hess Deep Rift: Conduits and seals in seafloor hydrothermal systems. *Geochemistry, Geophysics, Geosystems*, 8, Q10002. <https://doi.org/10.1029/2007GC001623>
- Karson, J., & Dick, H. (1983). Tectonics of ridge-transform intersections at the Kane Fracture Zone. *Marine Geophysical Research*, 6(1), 5198. <https://doi.org/10.1007/BF00300398>
- Leroy, S., Cannat, M., Momoh, E., Singh, S., Watremez, L., Sauter, D., et al. (2015). Anatomy of ultra-slow spreading Southwest Indian Ridge: The 2014 SISMOSMOOTH cruise. In AGU Fall Meeting Abstracts.
- Leroy, S., Lucazeau, F., d'Acremont, E., Watremez, L., Autin, J., Rouzo, S., et al. (2010). Contrasted styles of rifting in the eastern Gulf of Aden: A combined wide-angle, multichannel seismic, and heat flow survey. *Geochemistry, Geophysics, Geosystems*, 11, Q07004. <https://doi.org/10.1029/2009GC002963>

- Liner, C. L. (1990). General theory and comparative anatomy of dip moveout. *Geophysics*, 55(5), 595–607. <https://doi.org/10.1190/1.1442871>
- Little, T. A., Cox, S., Vry, J. K., & Batt, G. (2005). Variations in exhumation level and uplift rate along the oblique-slip Alpine fault, central Southern Alps, New Zealand. *Geological Society of America Bulletin*, 117(5–6), 707–723. <https://doi.org/10.1130/B25500.1>
- Loewenthal, D., Lu, L., Roberson, R., & Sherwood, J. (1976). The wave equation applied to migration. *Geophysical Prospecting*, 24(2), 380–399. <https://doi.org/10.1111/j.1365-2478.1976.tb00934.x>
- MacLeod, C. J., Escartin, J., Banerji, D., Banks, G. J., Gleeson, M., Irving, D. H. B., et al. (2002). Direct geological evidence for oceanic detachment faulting: The Mid-Atlantic Ridge, 15°45'N. *Geology*, 30(10), 879–882. [https://doi.org/10.1130/0091-7613\(2002\)0300879:DGEFOD2.0.CO;2](https://doi.org/10.1130/0091-7613(2002)0300879:DGEFOD2.0.CO;2)
- MacLeod, C. J., Searle, R., Murton, B., Casey, J., Mallows, C., Unsworth, S., & Harris, M. (2009). Life cycle of oceanic core complexes. *Earth and Planetary Science Letters*, 287(3), 333–344. <https://doi.org/10.1016/j.epsl.2009.08.016>
- Minshull, T., Muller, M., & White, R. (2006). Crustal structure of the Southwest Indian Ridge at 66°E: Seismic constraints. *Geophysical Journal International*, 166(1), 135–147. <https://doi.org/10.1111/j.1365-246X.2006.03001.x>
- Momoh, E., Cannat, M., Watremez, L., Leroy, S., & Singh, S. C. (2017). Quasi-3-D seismic reflection imaging, and wide-angle velocity structure of nearly amagmatic oceanic lithosphere at the ultra-slow spreading Southwest Indian Ridge. *Journal of Geophysical Research: Solid Earth*, 122, 9511–9533. <https://doi.org/10.1002/2017JB014754>
- Morris, A., Gee, J., Pressling, N., John, B., MacLeod, C. J., Grimes, C., & Searle, R. (2009). Footwall rotation in an oceanic core complex quantified using reoriented integrated ocean drilling program core samples. *Earth and Planetary Science Letters*, 287(1), 217–228. <https://doi.org/10.1016/j.epsl.2009.08.007>
- Muller, M. R., Minshull, T. A., & White, R. S. (1999). Segmentation and melt supply at the Southwest Indian Ridge. *Geology*, 27(10), 867–870. [https://doi.org/10.1130/0091-7613\(1999\)0270867:SAMSAT2.3.CO;2](https://doi.org/10.1130/0091-7613(1999)0270867:SAMSAT2.3.CO;2)
- Muller, M. R., Robinson, C., Minshull, T., White, R., & Bickle, M. (1997). Thin crust beneath ocean drilling program borehole 735b at the Southwest Indian Ridge? *Earth and Planetary Science Letters*, 148(1), 93–107. [https://doi.org/10.1016/S0012-821X\(97\)00030-7](https://doi.org/10.1016/S0012-821X(97)00030-7)
- Nedimovic, M. R., & West, G. F. (2003). Crooked-line 2D seismic reflection imaging in crystalline terrains: Part 1. Data processing. *Geophysics*, 68(1), 274–285. <https://doi.org/10.1190/1.1543213>
- Paquet, M., Cannat, M., Brunelli, D., Hamelin, C., & Humler, E. (2016). Effect of melt/mantle interactions on MORB chemistry at the easternmost Southwest Indian Ridge (6167e). *Geochemistry, Geophysics, Geosystems*, 17, 4605–4640. <https://doi.org/10.1002/2016GC006385>
- Parnell-Turner, R., Sohn, R. A., Peirce, C., Reston, T. J., MacLeod, C. J., Searle, R. C., & Simao, N. M. (2017). Oceanic detachment faults generate compression in extension. *Geology*, 45(10), 923–926. <https://doi.org/10.1130/G39232.1>
- Patriat, P., & Segoun, J. (1988). Reconstruction of the Central Indian Ocean. *Tectono-physics*, 155(1–4), 211–234. [https://doi.org/10.1016/0040-1951\(88\)90267-3](https://doi.org/10.1016/0040-1951(88)90267-3)
- Peron-Pinvidic, G., Shillington, D. J., & Tucholke, B. E. (2010). Characterization of sills associated with the U reflection on the Newfoundland margin: Evidence for widespread early post-rift magmatism on a magma-poor rifted margin. *Geophysical Journal International*, 182(1), 113–136. <https://doi.org/10.1111/j.1365-246X.2010.04635.x>
- Reston, T., Ruo, O., McBride, J., Ranero, C., & White, R. S. (1996). Detachment and steep normal faulting in Atlantic oceanic crust west of Africa. *Geology*, 24(9), 811–814. [https://doi.org/10.1130/0091-7613\(1996\)0240811:DASNFI2.3.CO;2](https://doi.org/10.1130/0091-7613(1996)0240811:DASNFI2.3.CO;2)
- Reston, T. J., Krawczyk, C., & Klaeschen, D. (1996). The S reflector west of Galicia (Spain): Evidence from prestack depth migration for detachment faulting during continental breakup. *Journal of Geophysical Research*, 101(B4), 8075–8091. <https://doi.org/10.1029/95JB03466>
- Reston, T. J., & McDermott, K. G. (2011). Successive detachment faults and mantle unroofing at magma-poor rifted margins. *Geology*, 39(11), 1071–1074. <https://doi.org/10.1130/G32428.1>
- Reston, T. (2018). Flipping detachments: The kinematics of ultraslow spreading ridges. *Earth and Planetary Science Letters*, 503, 144–157. <https://doi.org/10.1016/j.epsl.2018.09.032>
- Roumejon, S., & Cannat, M. (2014). Serpentinization of mantle-derived peridotites at mid-ocean ridges: Mesh texture development in the context of tectonic exhumation. *Geochemistry, Geophysics, Geosystems*, 15, 2354–2379. <https://doi.org/10.1002/2013GC005148>
- Sauter, D., Cannat, M., Rouméjon, S., Andreani, M., Birot, D., Bronner, A., et al. (2013). Continuous exhumation of mantle-derived rocks at the Southwest Indian Ridge for 11 million years. *Nature Geoscience*, 6(4), 314–320. <https://doi.org/10.1038/ngeo1771>
- Savage, H. M., & Brodsky, E. E. (2011). Collateral damage: Evolution with displacement of fracture distribution and secondary fault strands in fault damage zones. *Journal of Geophysical Research*, 116, B03405. <https://doi.org/10.1029/2010JB007665>
- Schindwein, V., & Schmid, F. (2016). Mid-ocean-ridge seismicity reveals extreme types of ocean lithosphere. *Nature*, 535(7611), 276–279. <https://doi.org/10.1038/nature18277>
- Schuba, C. N., Gray, G. G., Morgan, J. K., Sawyer, D. S., Shillington, D. J., Reston, T. J., & Jordan, B. E. (2018). A low-angle detachment fault revealed: Three-dimensional images of the S-reflector fault zone along the Galicia passive margin. *Earth and Planetary Science Letters*, 492, 232–238. <https://doi.org/10.1016/j.epsl.2018.04.012>
- Seher, T., Crawford, W. C., Singh, S. C., & Cannat, M. (2010). Seismic layer 2A variations in the Lucky Strike segment at the Mid-Atlantic Ridge from reflection measurements. *Journal of Geophysical Research*, 115, B03103. <https://doi.org/10.1029/2009JB006650>
- Smith, D. K., Cann, J. R., & Escartin, J. (2006). Widespread active detachment faulting and core complex formation near 13°N on the Mid-Atlantic Ridge. *Nature*, 442(7101), 440–443. <https://doi.org/10.1038/nature04950>
- Townend, J., Sutherland, R., Toy, V. G., Doan, M. L., Célérier, B., Massiot, C., et al. (2017). Petrophysical, geochemical, and hydrological evidence for extensive fracture-mediated fluid and heat transport in the Alpine faults hanging-wall damage zone. *Geochemistry, Geophysics, Geosystems*, 18, 4709–4732. <https://doi.org/10.1002/2017GC007202>
- Williams, J. N., Toy, V. G., Massiot, C., McNamara, D. D., Smith, S. A., & Mills, S. (2018). Controls on fault zone structure and brittle fracturing in the foliated hanging wall of the Alpine fault. *Solid Earth*, 9(2), 469. <https://doi.org/10.5194/se-9-469-2018>
- Xu, M., Canales, J. P., Tucholke, B. E., & DuBois, D. L. (2009). Heterogeneous seismic velocity structure of the upper lithosphere at Kane oceanic core complex, Mid-Atlantic Ridge. *Geochemistry, Geophysics, Geosystems*, 10, Q10001. <https://doi.org/10.1029/2009GC002586>
- Yilmaz, O. (2001). Seismic data analysis: Processing, inversion, and interpretation of seismic data. Society of Exploration Geophysicists. doi: <https://doi.org/10.1190/1.9781560801580>
- Yu, Z., Li, J., Liang, Y., Han, X., Zhang, J., & Zhu, L. (2013). Distribution of large-scale detachment faults on mid-ocean ridges in relation to spreading rates. *Acta Oceanologica Sinica*, 32(12), 109–117. <https://doi.org/10.1007/s13131-013-0397-y>